

# Yttrium-90 Quantitative Phantom Study Using Digital Photon Counting PET

**Joey Labour** (✉ [labour@creatis.insa-lyon.fr](mailto:labour@creatis.insa-lyon.fr))

Centre de Recherche en Acquisition et Traitement de l'Image pour la Santé <https://orcid.org/0000-0002-5602-3178>

**Philippe Boissard**

Centre Léon Bérard: Centre Leon Berard

**Thomas Baudier**

Centre Léon Bérard: Centre Leon Berard

**Fouzi Khayi**

Centre Léon Bérard: Centre Leon Berard

**David Kryza**

Centre Léon Bérard: Centre Leon Berard

**Pascale Veyrat Durebex**

Centre Léon Bérard: Centre Leon Berard

**Sandrine Parisse-Di Martino**

Centre Léon Bérard: Centre Leon Berard

**Thomas Mognetti**

Centre Léon Bérard: Centre Leon Berard

**David Sarrut**

Centre Léon Bérard: Centre Leon Berard

**Jean-Noël Badel**

Centre Léon Bérard: Centre Leon Berard

---

## Original research

**Keywords:** Radioembolisation, Digital photon counting, PET, Dosimetry, Monte Carlo simulation

**Posted Date:** January 15th, 2021

**DOI:** <https://doi.org/10.21203/rs.3.rs-144250/v1>

**License:**   This work is licensed under a Creative Commons Attribution 4.0 International License.

[Read Full License](#)

---

**Version of Record:** A version of this preprint was published at EJNMMI Physics on July 27th, 2021. See the published version at <https://doi.org/10.1186/s40658-021-00402-6>.

## PHYSICS

# Yttrium-90 quantitative phantom study using digital photon counting PET

Joey Labour<sup>1,2\*†</sup>, Philippe Boissard<sup>2†</sup>, Thomas Baudier<sup>1,2</sup>, Fouzi Khayi<sup>2</sup>, David Kryza<sup>2,3</sup>, Pascale Veyrat Durebex<sup>2</sup>, Sandrine Parisse-Di Martino<sup>2</sup>, Thomas Mognetti<sup>2</sup>, David Sarrut<sup>1,2†</sup> and Jean-Noël Badel<sup>1,2†</sup>

\*Correspondence:

labour@creatis.insa-lyon.fr

<sup>1</sup>CREATIS; CNRS UMR 5220; INSERM U 1044; Université de Lyon; INSA-Lyon; Université Lyon 1, Lyon, France

Full list of author information is available at the end of the article

†Equal contributor

## Abstract

**Background:** PET imaging of <sup>90</sup>Y-microspheres distribution following radioembolisation is a challenging task due to the count-starved statistics from the low branching ratio producing e<sup>+</sup>/e<sup>-</sup> pairs during <sup>90</sup>Y decay. The recent PET systems using silicon photo-multipliers technology has shown better <sup>90</sup>Y image quality compared to photo-multiplier tubes. The aim of the present study was to quantitatively evaluate the impact of <sup>90</sup>Y imaging conditions and reconstruction parameters on the dosimetry calculations using a digital photon counting PET.

**Methods:** Quantitative PET and dosimetry accuracy were evaluated using two uniform cylindrical phantoms specific for PET calibration validation. A body phantom with an 9:1 hot sphere-to-background ratio was scanned at different activity concentrations of <sup>90</sup>Y. Reconstructions were performed using OSEM algorithm with varying parameters. Time-of-flight and point-spread function modellings were included in all reconstructions. Absorbed dose calculations were carried out using Voxel S-Values convolution and were compared to reference Monte Carlo simulations. Dose-volume histograms and root-mean-square deviations were used to evaluate reconstruction parameter sets. Thanks to listmode data, datasets for phantoms and patients were rebinned into varying lengths of time to assess the influence of acquisition duration on the calculation of absorbed dose.

**Results:** A 2 mm full width at half maximum post-reconstruction Gaussian filter size can be used for image reconstruction, keeping the same accuracy as when no filter is applied for dosimetry purposes and reducing noise. Larger filter sizes should not be used. An acquisition duration of more than 10 min/bed reduces image noise but has no significant impact in the quantification of phantom and patient data for the digital photon counting PET. 3 iterations with 10 subsets was found suitable for large spheres whereas 1 iteration with 30 subsets could improve dosimetry for smaller spheres.

**Conclusion:** The choice of iterations and subsets combination depends on the size of the spheres. However, one should be careful on this choice, depending on the imaging conditions and setup. This study can be useful in this choice for future studies for more accurate <sup>90</sup>Y post-dosimetry using a digital photon counting PET.

**Keywords:** Radioembolisation; Digital photon counting; PET; Dosimetry; Monte Carlo simulation

## 1 Background

Liver radioembolisation or selective internal radiation therapy (SIRT) is an intra-arterial method used in clinical practice to treat unresectable hepatic malignan-

cies [1, 2]. Currently, SIRT can be performed either with  $^{90}\text{Y}$  or  $^{166}\text{Ho}$  microspheres. During  $^{90}\text{Y}$ -SIRT, the high energy  $\beta$ - emitter  $^{90}\text{Y}$  particles which are encapsulated in resin or glass microspheres, are administered through selected branches of the hepatic artery which feed the tumours. This method ensures a regional biodistribution of the  $^{90}\text{Y}$ -microspheres delivering a highly localised absorbed dose to the perfused regions, sparing nearby organs at risk and healthy tissues with the advantage of a negligible radiation burden to both non-embolized portions and extrahepatic tissues. The  $^{90}\text{Y}$ -SIRT method is widely used owing to its clinical efficacy and relative safety [1–5].

At present, the prediction of the biodistribution of  $^{90}\text{Y}$ -microspheres is generally performed using  $^{99m}\text{Tc}$ -labelled macro-aggregated albumin (MAA), prior to treatment. However,  $^{99m}\text{Tc}$ -MAA biodistribution does not always match with post-therapy  $^{90}\text{Y}$ -microspheres distribution [6–9] and radionuclide biodistribution assessment must be performed following treatment either by single-photon emission computed tomography (SPECT) or positron emission tomography (PET). This assessment is mainly done to prevent any complication related to possible extrahepatic deposition of microspheres and determine the intrahepatic microspheres distribution over the perfused tumorous and non-tumorous liver tissue.

$^{90}\text{Y}$  SPECT imaging exploits bremsstrahlung gammas, with various published energy windows [10] and has been used for post-SIRT treatment evaluation [11]. However, SPECT suffers from noise and challenging quantitative analysis. Alternatively,  $^{90}\text{Y}$  PET imaging exploits a minor positron decay [12–17]. In 2004, Nickles *et al.* [18] first exploited this property to show the distribution of the regional absorbed dose delivered by  $^{90}\text{Y}$  therapies using PET, although difficult and time-consuming due to the count-starved statistics for annihilation photons. Activity distribution assessment after  $^{90}\text{Y}$ -SIRT was proved feasible in 2010 by Lhommel *et al.* [19, 20] with the help of time-of-flight (ToF) information added on PET/CT systems. Other studies followed and showed that ToF PET compared to non-ToF PET provided improved recovery in reconstructed quantitative data [19–25], outperforming at the same time  $^{90}\text{Y}$  bremsstrahlung SPECT [11, 21]. In 2007, Selwyn *et al.* [16] verified the branching ratio related to  $e^+/e^-$  pair production during  $^{90}\text{Y}$  decay to be  $(31.86 \pm 0.47) \times 10^{-6}$ , following de-excitation from the  $0^+$  excited state of  $^{90}\text{Zr}$ . The latest published value was from Dryák and Šolc [17] in 2020, who measured the branching ratio to be  $(32.6 \pm 0.4) \times 10^{-6}$ .

The recent digital PET systems are equipped with silicon photo-multipliers (SiPM) technology that replaces conventional photo-multiplier tubes (PMT). They allow enhanced ToF capability and coincidence timing resolution owing to faster and more compact electronics [26, 27]. They demonstrate better performances for sensitivity, spatial resolution, count rates and overall image quality [28–32].

Following literature, assessments for  $^{90}\text{Y}$  imaging were performed largely using criteria based on NEMA guidelines [33] and by evaluating detectability for diagnostic purposes rather than dosimetry calculations. In 2013, Willowson *et al.* [34] and Carlier *et al.* [22] showed that with the help of ToF information, higher detectability was reached with a small number of Ordered Subsets Expectation Maximisation (OSEM) iterations on Siemens Biograph mCT systems. Few studies evaluated OSEM reconstruction parameters using absorbed dose calculation tools. In 2014,

Pasciak *et al.* [35] based on previous findings [22, 34] found that an additional 4.5 mm full width at half maximum (FWHM) point-spread function (PSF) modelling improved accuracy in absorbed dose distributions using dose-volume histograms (DVH). In 2018, Siman *et al.* [36] studied a GE D690 PET/CT and found that 3 iterations with 12 subsets with additional PSF modelling and a 5.2 mm FWHM post-reconstruction Gaussian filter size provided the least root-mean-square deviation (RMSD) between their experimental and reference DVH.

This study focuses on the use of a DPC (Digital Photon Counting)-PET for  $^{90}\text{Y}$  quantification and dosimetry purposes following SIRT. We considered the fully digital Philips VEREOS PET SiPM system, with a 1:1 coupling between the lutetium–yttrium oxyorthosilicate (LYSO) scintillator crystals and the SiPM [28], showing improved timing resolution and signal-to-noise ratio (SNR) compared to conventional PMT-PET [37]. Wright *et al.* [38–40] showed that DPC-PET detection of annihilation photons following  $^{90}\text{Y}$ -SIRT is feasible, showing concordant visualisation with improved  $^{90}\text{Y}$ -to-background contrast of microspheres distribution with the DPC-PET compared to SPECT and PMT-PET systems.

OSEM reconstruction parameters evaluations from previous studies [22, 34–36] were performed on PMT-PET systems with ToF resolutions around 550 ps. Therefore, suggested parameters in literature might not be suitable for the DPC-PET with a ToF resolution around 300 ps [28–30], due to the dependence of the convergence of OSEM-based algorithms to the ToF information [37]. Moreover, implementations of OSEM-based algorithms differ within systems and the OSEM algorithm implemented in the DPC-PET is based on listmode data, instead of sinograms, and use spherically symmetric volume elements to model the image, instead of voxels [41, 42].

In this study, we investigated the accuracy of  $^{90}\text{Y}$  DPC-PET by the evaluation of OSEM reconstruction parameters and acquisition duration to estimate the absorbed dose distribution based on DVH [43], as proposed by Siman *et al.* [36].

## 2 Materials and methods

In order to evaluate the accuracy of image-based absorbed dose estimations from  $^{90}\text{Y}$  DPC-PET, 3 phantoms were selected and used in various conditions. Acquired PET images were used as input activity maps to compute the absorbed dose distributions and DVH. Obtained dosimetry were compared to reference absorbed dose distributions computed with Monte Carlo and the impact of several parameters, volumes of interest (VOI), activity levels, reconstruction parameters and acquisition duration, were evaluated. In the following subsections, we describe 1) the phantoms, 2) the acquisition and reconstruction parameters, 3) the algorithms used to compute the absorbed dose, 4) the figures of merit and 5) the clinical application using several patient image datasets acquired on the same DPC-PET following  $^{90}\text{Y}$ -SIRT treatment.

### 2.1 Phantoms and activities

A 6800 mL uniform cylindrical phantom (Ph1) and a 300 mL fillable insert in a cylindrical phantom (Ph2), were used for validation of quantitative recovered data following PET calibration for  $^{90}\text{Y}$ , as shown in Figures 1A and 1B, respectively.

A NEMA IEC body phantom (Ph3) in Figure 1C, was then used for quantitative measurements for dosimetry evaluations, consisting of a background compartment of approximately 9700 mL, a lung insert and an insert with six fillable spheres of varying diameters of 10, 13, 17, 22, 28 and 37 mm. The corresponding nominal volumes of the spheres ranged between 0.52 and 26.52 mL. This choice of phantoms allowed to know the reference activities and to compute the reference absorbed dose distributions for various VOI sizes.

Prior to phantom preparations, a volume of 100  $\mu\text{L}$  diethylenetriaminepentaacetic acid (DTPA) at a concentration of 5  $\text{mg}\cdot\text{mL}^{-1}$  was added to two vials containing 2850 MBq of  $^{90}\text{YCl}_3$  in 1.03 mL solution, each. This was done to prevent the known effect of adsorption of  $^{90}\text{YCl}_3$  on the inner PMMA walls of plastic phantoms which may negatively affect PET quantitative imaging studies [44]. Prepared syringes used for filling Ph1, Ph2 and Ph3 were flushed several times to make sure all the activity has been injected in different phantom parts. All syringes were also measured for residual activities and accounted in activity calculations.

*Cylindrical phantoms, Ph1 and Ph2.* Ph1 was filled with 2130 MBq of  $^{90}\text{YCl}_3$  in water. The 300 mL water insert in Ph2 was filled with a total activity of 540 MBq of  $^{90}\text{YCl}_3$  in a cold water background. The reference initial activity concentrations ( $AC_{ref}$ ) measured with a dose calibrator were 0.31  $\text{MBq}\cdot\text{mL}^{-1}$  and 1.83  $\text{MBq}\cdot\text{mL}^{-1}$  at injection, for Ph1 and Ph2 insert, respectively.

*NEMA IEC body phantom, Ph3.* A stock solution was prepared for filling the spheres by injecting 225 MBq of  $^{90}\text{YCl}_3$  in 100 mL of water. An activity of 2355 MBq of  $^{90}\text{YCl}_3$  was added to the 9700 mL water background. The  $AC_{ref}$  in the spheres and background compartment were 2.25  $\text{MBq}\cdot\text{mL}^{-1}$  and 0.24  $\text{MBq}\cdot\text{mL}^{-1}$  at injection, respectively. A sphere-to-background ratio (SBR) of 9:1 was obtained, close to like in the QUEST study [44].

Image acquisitions for all phantoms were performed over six consecutive days (two radioactive periods) to account for the response of the PET with decreasing activity concentrations. Markers were placed to allow for reproducible placement of the phantoms between daily scans. Data acquisitions were performed in listmode format. The acquisition durations were 30 minutes per bed (min/bed) for both Ph1 and Ph2 and 15 min/bed for Ph3.

All image reconstructions were performed with ToF information and using relaxed List Mode Ordered Subset Expectation Maximisation (LMOSEM) algorithm [41] implemented on Philips PET systems, with isotropic voxels of  $2 \times 2 \times 2 \text{ mm}^3$ . They were post-treated with a regularised version of the Richardson-Lucy algorithm for resolution recovery [45, 46] with the default recommended parameters of the PSF modelling (1 iteration and 6 mm regularisation kernel) which provide reasonable contrast recovery without noticeable Gibbs artefacts [42, 47].

Listmode data for Ph1 and Ph2 were reconstructed with *Recon1*, the default clinical setup recommended by Philips, see Table 1. Several parameters were compared for Ph3. The number of iterations were fixed to 1, 2 or 3 to limit image noise amplification. The number of subsets were varied with 10, 20 or 30 subsets to cover the range of suggested number of subsets in previous studies [22, 34–36, 44, 48–61].

Post-reconstruction Gaussian filters were applied with varying sizes between 0 (no filter) and 8 mm FWHM with increments of 2 mm. In total, 45 combinations for reconstructions were compared for Ph3. Reconstruction parameter sets suggested from literature were also tested, *Recon2* [36] and *Recon3* [22, 34, 35], see Table 1. Reconstruction parameter sets are denoted i3s5-2mm for example for 3 iterations with 5 subsets and a 2 mm FWHM post-reconstruction Gaussian filter.

Reconstruction parameter set	Iterations	Subsets	Gaussian filter (mm @ FWHM)	PSF	ToF
<i>Recon1</i>	3	5	2	Yes	Yes
<i>Recon2</i>	3	12	5.2	Yes	Yes
<i>Recon3</i>	1	21	5	Yes	Yes

**Table 1** Parameter sets used for listmode data reconstructions.

Finally, thanks to listmode data, datasets for Ph3 were rebinned into varying acquisition durations, from 5 to 15 min/bed, in order to evaluate the impact of the counts statistics and investigate if shorter acquisition durations might be used.

## 2.2 Absorbed dose computation

Monte Carlo simulations were used to estimate the reference absorbed dose distributions in the 3 phantoms according to the known  $AC_{ref}$  at injection. These reference absorbed dose distributions were compared to the ones that can be estimated from the  $^{90}\text{Y}$  PET images. These image-based absorbed dose computations were performed with Voxel S-Values (VSV) kernel based convolution method considering  $^{90}\text{Y}$  PET images as input activity maps, as it can be done in clinical conditions.

*Reference absorbed dose.* Monte Carlo simulations were performed with the Geant4 Application for Tomographic Emission (GATE) platform 9.0 [62, 63] using GEANT4 10.5 [64]. The geometry, dimensions and material composition of each phantom were modelled. The modelled geometry for Ph3 is shown in Figure 1D. The physics list named `emstandard_opt4` was used<sup>[1]</sup>. It contains the GEANT4 most accurate standard and low-energy models for electromagnetic processes recommended for medical applications [65]. Range production cuts were set to 1 mm for electrons and photons in the whole geometry. In GEANT4, it means that secondary particles are only created and tracked when their expected range in the current material is larger than this distance. No variance reduction technique was used. The  $\beta$ -radioactive sources of  $^{90}\text{Y}$  were simulated by homogeneous *generic ion sources* in each sphere and the background compartment. The absorbed dose was scored with  $2 \times 2 \times 2 \text{ mm}^3$  voxels sizes. About  $6 \times 10^5$  primary particles were used to reach less than 1% statistical Type-A uncertainty in all VOI of the different phantoms. Final absorbed dose values were scaled according to the known accumulated activities in all injected regions.

*Image-based absorbed dose.* Absorbed dose distributions were computed from the PET images with DOSIsoft® (Cachan, France) with the VSV dose kernel convolution algorithm following the MIRD formalism [66–68]. The VSV convolution approach was chosen instead of the Local Deposition Method (LDM) also available

<sup>[1]</sup>See <https://geant4.web.cern.ch/node/1731>

in the software. It is considered as a compromise between more simplified calculation models and Monte Carlo calculations and allows to achieve better absorbed dose distribution information in the clinical environment [67–71].

*Partition model.* Mean absorbed dose estimations were also performed with the simplified MIRD formalism ( $D_{MIRD}$ ) for  $^{90}\text{Y}$ , using the partition model [72], according to:

$$D_{MIRD} = \frac{A(\text{GBq})}{M(\text{kg})} \times 49.67 \quad (1)$$

where  $A$  is the total activity at injection in each VOI and  $M$  is the mass of the VOI.

### 2.3 Dosimetry-based figures of merit

VOI were defined on the CT images of the different phantoms, as the whole volume for Ph1 and as the cylindrical contour for the insert in Ph2. For Ph3, spherical VOI were defined for the 6 spheres using the exact internal diameter of each sphere.

The DVH of each sphere, were computed as suggested in [36]. The reference Monte Carlo and image-based VSV DVH are denoted  $DVH_{ref}^{MC}$  and  $DVH_{pet}^{VSV}$ , respectively. For each parameter set  $r$  used for image reconstruction and sphere size  $\varnothing$ , differences between the absorbed dose distributions were evaluated by the RMSD between their respective  $DVH_{ref}^{MC}$  and  $DVH_{pet}^{VSV}$ , see equation 2.

$$RMSD_{\varnothing,r} = \sqrt{\frac{\sum_{i=0}^{N-1} (DVH_{ref,\varnothing,i}^{MC} - DVH_{pet,\varnothing,r,i}^{VSV})^2}{N}} \quad (2)$$

with  $N$  samples for each corresponding pair of reference and PET-based DVH. In addition, instead of the NEMA contrast recovery coefficient (CRC) definition [33] that aims at lesion detection rather than absorbed dose estimation, we used the mean activity concentration recovery coefficient ( $RC_{AC}$ ) and the absorbed dose recovery coefficient ( $RC_{Dose}$ ) for quantitative analysis with decreasing activity concentration, see equations 3 and 4.

$$RC_{AC,\varnothing} = \frac{AC_{pet,\varnothing}}{AC_{ref,\varnothing}} \quad (3)$$

$$RC_{Dose,\varnothing} = \frac{D_{pet,\varnothing}^{VSV}}{D_{ref,\varnothing}^{MC}} \quad (4)$$

where for each sphere size  $\varnothing$ ,  $AC_{pet,\varnothing}$  is the mean activity concentration measured from output PET images,  $AC_{ref,\varnothing}$  is the reference activity concentration (here at the start of each acquisition),  $D_{pet,\varnothing}^{VSV}$  is the PET imaged-based mean absorbed dose and  $D_{ref,\varnothing}^{MC}$  is the mean absorbed dose calculated from the reference Monte Carlo simulations.

## 2.4 Clinical application

The dosimetric impact of reducing PET acquisition duration was investigated on five patients treated by  $^{90}\text{Y}$ -SIRT in our hospital, see Table 2. The initial acquisition duration was 15 min/bed position. Listmode datasets were used to decrease artificially the acquisition duration down to 10 and 5 min/bed position at the step of PET images reconstruction. Images were reconstructed using parameters chosen following phantom data evaluation in this study.

Different VOI were defined by an experimented clinician by manual 3D segmentations of the (1) total liver, (2) perfused liver, (3) tumor and (4) healthy perfused liver. Figures 1E and 1F depict axial slices of liver VOI segmentations for patients #2 and #3, respectively. DVH analysis were performed on the different VOI, using the VSV convolution algorithm implemented in DOSIsoft®.

Patient	Sex	Age (years)	Tumor type	Microsphere	Injected $^{90}\text{Y}$ activity (GBq)
#1	M	65	HCC	Glass	2.463
#2	F	92	HM	Resin	0.716
#3	M	67	HM	Resin	0.800
#4	F	16	HCC	Resin	1.752
#5	F	67	HM	Resin	1.479

**Table 2** Patients' characteristics

*HCC* Hepatocellular carcinoma, *HM* hepatic metastases

## 3 Results

### 3.1 Cylindrical phantoms Ph1 and Ph2

The first test was a sanity check to evaluate the PET response. Figure 2A depicts the measured activity concentrations from reconstructed PET images  $AC_{pet}$ , versus  $AC_{ref}$ , initially measured with a dose calibrator, for both Ph1 and Ph2. Measured  $AC_{ref}$  ranged from 0.08 to 0.29 MBq.mL $^{-1}$  for Ph1, and from 0.49 to 1.71 MBq.mL $^{-1}$  for Ph2. The maximum absolute differences between  $AC_{pet}$  and  $AC_{ref}$  were 0.01 and 0.04 MBq.mL $^{-1}$  for Ph1 and Ph2, respectively.

Figures 2B and 2C depict the calculated DVH for Ph1 and Ph2, respectively, according to the computation methods used:  $DVH_{ref}^{MC}$  (reference absorbed dose by Monte Carlo simulation) or  $DVH_{pet}^{VSV}$  (PET image-based absorbed dose by VSV convolution). The obtained DVH illustrate the loss of accuracy brought by the use of images in the calculation of absorbed dose distributions.

Table 3 provides the mean absorbed dose ( $D_{mean}$ ), the absorbed dose at 50% volume ( $D_{50}$ ) computed with each method and their differences in percent (Diff. (%)) for both phantoms.

Dose criterion	Ph1: 6800 mL cylindrical			Ph2: 300 mL insert		
	Ref. MC (Gy)	VSV (Gy)	Diff. (%)	Ref. MC (Gy)	VSV (Gy)	Diff. (%)
$D_{mean}$	15.1	14.3	-5.3	83.7	71.8	-14.2
$D_{50}$	15.2	13.4	-11.8	89.2	76.4	-14.3

**Table 3** Comparison of dose calculation methods through the  $D_{mean}$  and  $D_{50}$  for Ph1 at 0.29 MBq.mL $^{-1}$  and Ph2 at 1.71 MBq.mL $^{-1}$ .

### 3.2 NEMA IEC body phantom Ph3

In this section, we proceed in the comparison of different reconstruction parameters using DVH and RMSD at  $AC_{ref}$  equal to  $2.18 \text{ MBq.mL}^{-1}$  for Ph3. We also evaluate the effect of acquisition duration on absorbed dose distributions. The response of the PET is then evaluated using the  $RC_{AC}$  and  $RC_{Dose}$  for different  $AC_{ref}$  over two  $^{90}\text{Y}$  radioactive periods following phantom preparation.

#### 3.2.1 Evaluation using DVH

In total, 270 image-based  $DVH_{pet}^{VSV}$  (45 reconstruction parameter sets described in section 2.1 times 6 sphere sizes) have been computed, and 6 reference  $DVH_{ref}^{MC}$  corresponding to each sphere have been simulated. For each sphere and each reconstruction, the  $DVH_{pet}^{VSV}$  has been compared to the  $DVH_{ref}^{MC}$ .

Figure 4 depicts the simulated  $DVH_{ref}^{MC}$  (black curves) for each sphere and the  $DVH_{pet}^{VSV}$  for 8 reconstructions per sphere (only extremes are depicted: 1 and 3 iterations, 10 and 30 subsets, 0 and 8 mm FWHM filter).

*Varying post-reconstruction Gaussian filter.* As expected for all spheres, increasing the filter size reduced the maximum absorbed dose ( $D_{max}$ ) of the  $DVH_{pet}^{VSV}$ , e.g. between i1s30-0mm and i1s30-8mm or any other corresponding pair in Figure 4. It could be observed that a too large filter could not be suitable for dosimetry, specially with decreasing sphere sizes where the area under the curve can be significantly reduced (comparing cyan and green  $DVH_{pet}^{VSV}$  in Figures 4D, 4E and 4F).

*Varying subsets.* As expected, increasing the number of subsets had the adverse effect for all spheres, increasing the  $D_{max}$  of the  $DVH_{pet}^{VSV}$ , e.g. between i3s10-0mm and i3s30-0mm or any other corresponding pair in Figure 4. For the largest 28 and 37 mm spheres, 30 iterations compared to 10 iterations favoured noise amplification to the detriment of intermediate absorbed doses (comparing red and blue  $DVH_{pet}^{VSV}$ ).

*Varying iterations.* The relationship in varying the number of iterations was less clear and intuitive than with the number of post-reconstruction filter or subsets. For spheres  $> 20$  mm (22, 28 and 37 mm), increasing the number of iterations did not incur significant change in the shape of the  $DVH_{pet}^{VSV}$  or resulted in a slight increase in the  $D_{max}$ , e.g. between i1s10-0mm and i3s10-0mm or any other corresponding pair in Figure 4. Increasing iterations from 1 to 3 did not seem to favour noise amplification for the biggest spheres. On the other hand, more variations were observed for spheres  $< 20$  mm (10, 13, 17 mm) using the same comparison, e.g. between i1s10-0mm and i3s10-0mm.

*Equivalent updates.* Equivalent number of updates (product of the number of iterations and subsets) did not provide the same accuracy in  $DVH_{pet}^{VSV}$  as it would be expected, e.g. between i1s30-0mm and i3s10-0mm or between i1s30-8mm and i3s10-8mm.

### 3.2.2 Comparison using RMSD

Figure 3A outlines the RMSD between  $DVH_{pet}^{VSV}$  and  $DVH_{ref}^{MC}$  for the 28 mm sphere as an example, corresponding to 45 reconstructions (9 reconstruction parameter sets times 5 filter sizes). The figure also shows three additional RMSD values for *Recon1-3* in Table 1. Independently of the combination of iterations and subsets, the RMSD between  $DVH_{pet}^{VSV}$  and  $DVH_{ref}^{MC}$  were at lowest when no (0 mm), or a 2 mm FWHM post-reconstruction Gaussian filter was applied. Similar observations were made for all spheres, except for the 22 mm sphere where the  $D_{max}$  could be amplified when no filter was applied, and met the ones made in Figure 4 when increasing the filter size.

From the previous findings, we now consider the use of a post-reconstruction Gaussian filter size of 2 mm FWHM for dosimetry, which can reduce noise in the reconstructed image by keeping the same accuracy as when no filter is applied. Figure 3B depicts the RMSD for all spheres obtained for reconstructions with a 2 mm FWHM filter only. Larger variations in RMSD were found for spheres < 20 mm than spheres > 20 mm. For the 10 to 17 mm spheres, i1s30-2mm provided the smallest RMSD. For the 22 to 37 mm spheres, the smallest RMSD were obtained using two combinations: i3s10-2mm for both the 22 and 28 mm spheres, and i1s20-2mm for the 37 mm sphere.

### 3.2.3 Effect of acquisition duration

Figure 5 depicts the effect of the acquisition duration on the  $DVH_{pet}^{VSV}$ , for the 6 spheres of Ph3. Reconstructions were performed with i3s10-2mm selected from the previous sections, providing a good compromise in reducing  $D_{max}$  and providing more accurate intermediate absorbed doses for the larger spheres (22-37 mm in Figure 4). The RMSD between  $DVH_{pet}^{VSV}$  for a 15 and a 10 min/bed acquisitions were 3.2, 8.0, 1.6, 1.8, 23.2 and 19.4 for the 37 to 10 mm spheres, respectively. These corresponding RMSD increased to 10.1, 12.7, 5.6, 6.8, 43.6 and 24.2, when comparing a 15 to a 5 min/bed  $DVH_{pet}^{VSV}$ , respectively.

### 3.2.4 $RC_{AC}$ and $RC_{Dose}$

Table 4 provides a comparison for Ph3 between the  $D_{mean}$  obtained with different calculation methods ( $D_{MIRD}$ ,  $D_{ref}^{MC}$  and  $D_{pet}^{VSV}$ , see section 2.2) and their corresponding  $D_{50}$ , at the image acquisition with the highest  $AC_{ref}$  equal to 2.18 MBq.mL<sup>-1</sup>. As expected,  $D_{ref}^{MC}$  decreased with decreasing sphere sizes since the sphere surface-to-volume ratio increases, leading to more absorbed dose delocalisation due to electrons exiting the spherical VOI. Moreover,  $D_{pet}^{VSV}$  dropped when estimated from the PET image compared to the reference absorbed dose, e.g. from 89.5 Gy to 59.8 Gy for the 17 mm sphere.  $D_{mean}$  and  $D_{50}$  were comparable for each calculation method.

The previous results were obtained for a given  $AC_{ref}$ , but results might vary at other activity levels. Figures 6A and 6B depict the  $RC_{AC}$  and  $RC_{Dose}$  (see equations 3 and 4) for all the spheres with decreasing  $AC_{ref}$ , respectively.  $AC_{ref}$  ranged between 0.61 and 2.18 MBq.mL<sup>-1</sup>. All reconstructions were performed with i3s10-2mm.

Recovery of information is influenced by activity concentration present in the FOV of the PET.  $RC_{AC}$  and  $RC_{Dose}$  decrease with decreasing  $AC_{ref}$  in the spheres. On

VOI	$D_{MIRD}$	Monte Carlo simulations		VSV convolution	
		$D_{ref}^{MC}$	$D_{50,ref}^{MC}$	$D_{pet}^{VSV}$	$D_{50,pet}^{VSV}$
$\varnothing_{10mm}$	114.2	73.3	66.1	26.8	17.3
$\varnothing_{13mm}$	114.2	81.1	77.4	46.3	45.3
$\varnothing_{17mm}$	114.2	89.5	86.8	59.8	55.9
$\varnothing_{22mm}$	114.2	93.8	95.2	89.2	81.0
$\varnothing_{28mm}$	114.2	97.8	101.1	79.7	80.5
$\varnothing_{37mm}$	114.2	101.8	105.8	80.5	80.0

**Table 4** Comparison between absorbed dose estimations for all spheres ( $\varnothing_{imm}$ ). All values in the table are in Gy.

overall,  $RC_{AC}$  and  $RC_{Dose}$  were comparable for all spheres and  $AC_{ref}$ .  $RC_{Dose}$  was slightly greater than  $RC_{AC}$  for most of the corresponding points between Figures 6A and 6B.

### 3.3 Clinical application

Figure 7 shows the influence of acquisition duration on the absorbed dose distributions for post  $^{90}\text{Y}$ -SIRT patient acquisitions. Few differences were observed between  $DVH_{pet}^{VSV}$  calculated from 10 and 15 min/bed acquisitions, for each liver VOI defined for all 5 patients. The RMSD between 10 and 15 min/bed acquisition for patient #1 were 0.3, 1.2, 1.5 and 0.9 for the total liver, perfused liver, tumor and healthy perfused liver VOI, respectively. The corresponding RMSD between 5 and 15 min/bed acquisitions for patient #1 increased to 2.8, 18.3, 12.4 and 24.1, respectively.

Due to the size of the liver, post  $^{90}\text{Y}$ -SIRT patients generally undergo a 2×15 min/bed acquisition in our hospital. The reduction of acquisition durations on the specific patients studied here seemed to have no significant impact on dosimetry via  $DVH_{pet}^{VSV}$ . Also, the visual interpretation made by physicians were similar when comparing 10 to a 15 min/bed patient acquisitions. We can therefore suggest a reduction of the acquisition duration from 15 to 10 min/bed, performing a total of 20 minutes instead of 30 minutes for 2 bed positions, helping in improving patient comfort.

## 4 Discussion

*Context.* The main goal of this work was to evaluate the influence of imaging conditions and reconstruction parameters using a DPC-PET to improve  $^{90}\text{Y}$  dosimetry calculations. A sanity check was first performed using two cylindrical uniform phantoms. A NEMA IEC body phantom was used to evaluate the relaxed LMOSEM algorithm parameters implemented in Philips reconstruction platforms for PET imaging. OSEM parameters were varied to find combinations of iterations, subsets and post-reconstruction Gaussian filter sizes which would provide the least difference between the  $DVH_{ref}^{MC}$  using GATE and  $DVH_{pet}^{VSV}$  using DOSIsoft® (Cachan, France). ToF and PSF modellings were considered in all reconstructions without exception. The acquisition duration was varied by rebinning listmode datasets to suggest the smallest duration that an image acquisition can be made with acceptable accuracy degradation using both phantom and patient data. A method suggested by Siman *et al.* using RMSD between our  $DVH_{ref}^{MC}$  and  $DVH_{pet}^{VSV}$  was used. No special intent was made towards improving image quality using NEMA standards [33] since the goal was to emphasise on the improvement of dosimetry accuracy.

*Ph1 and Ph2.* The DPC-PET provided accurate results with large phantoms, Ph1 and Ph2. Good agreements were obtained between the mean activity concentration measured in the output PET image,  $AC_{pet}$ , and the reference  $AC_{ref}$  as shown in Figure 2A, suggesting an adequate calibration of our DPC-PET for  $^{90}\text{Y}$  imaging for the range of activity concentrations studied. However, differences were obtained in calculations of absorbed dose distributions comparing  $DVH_{ref}^{MC}$  and  $DVH_{pet}^{VSV}$  as shown in Figures 2B and 2C for Ph1 and Ph2, illustrating the loss of accuracy brought by the use of the PET images compared to the ideal reference Monte Carlo simulations. This might be due to the low statistics and noise conditions in which imaging was performed which could cause heterogeneity in the activity distribution and therefore in the absorbed dose distribution.

*Ph3.* The differences in  $DVH_{ref}^{MC}$  and  $DVH_{pet}^{VSV}$  are also depicted in Figures 4, 3 and 5 where the size of the smaller spheres of *Ph3* became a limit for good accuracy, showing  $DVH_{pet}^{VSV}$  and RMSD which have large variations depending on the reconstruction parameters used. Siman *et al.* also showed relative large RMSD between their reference and PET image-based DVH, illustrating the loss of accuracy brought by the use of the images. Figures 5E and 5F depict the limit of reducing acquisition duration for small lesions. RMSD between a 10 to a 15 min/bed acquisitions were significant for the 10 and 13 mm spheres compared to the other 4 larger spheres. On the other hand, acquisition duration can be reduced to 10 min/bed using a DPC-PET if the size of the lesion is at least 17 mm in diameter based on the obtained absorbed dose distributions in this study. The results reported from phantom to patient data confirmed few differences in  $DVH_{pet}^{VSV}$  between a 10 and a 15 minutes acquisition duration, as depicted in Figure 7.

*Evaluation through DVH.* The evaluation of the reconstruction parameters for dosimetry is necessary from system to system, first owing to different PET performances in terms of sensitivity, spatial resolution, counts rates, energy and timing resolutions [29, 30, 33, 73, 74]. Second, for different reconstruction algorithms, e.g. the OSEM or Bayesian Penalised Likelihood (BPL), where in our case, the implementations of OSEM-based algorithms vary from one constructor to another, and third for the very specific configurations of imaging protocols from one hospital to another.

The choice of a combination of parameters for OSEM reconstructions is not simple and is specific for one configuration of SBR,  $AC_{ref}$ , image voxel size and lesion size. In our study, the variation of iterations limited from 1 to 3 did not have a significant impact on the calculated absorbed dose distributions, see Figure 4. On the other hand, varying subsets and the FWHM of the post-reconstruction Gaussian filter had an impact. The use of 30 subsets could help in improving accuracy in dosimetry for the small spheres, but could favour noise amplification in the image compared to 10 subsets. The number of updates, which is the product of the number of iterations and subsets was not used as objective criteria for evaluation since different combinations for the same number of updates could provide different results, e.g. 30 updates for both i1s30-0mm and i3s10-0mm in Figure 4.

Ref.	Scanner	Spheres phantom set					
		SBR	$AC_{ref}$ (MBq.mL <sup>-1</sup> )	Contrast	Activity	Dose	Optim. (Variable parameters)
Werner et al. [48]	Biograph Hi-Rez 16 Gemini TF	N/A	3.6	-	x	-	-
Van Elmbt et al. [49]	Gemini Power 16 Ecat Exact HR+	3:1	1.3	-	x	-	-
Bagni et al. [50] D'Arienzo et al. [51]	Discovery ST	10:1	1.92	-	x	-	-
Willowson et al. [34]	Biograph mCT-S(64)	8:1	3.9	x	x	-	OSEM (i1, i2, i3, s14, s21, s24)
Elschot et al. [52]	Biograph mCT	1:0 9:1	2.4	x	-	x	-
Carrier et al. [22]	Biograph mCT 40	40:1	8.1	-	x	-	OSEM (i1, i3)
Attarwala et al. [53]	Biograph mCT 40	8:1	2.38	-	x	-	OSEM (i1 to i12)
Martí-Climent et al. [54]	Biograph mCT-TrueV	5:1	1	x	-	-	OSEM (i1, i2, i3, 2mm, 4mm, 6mm)
Pasciak et al. [35]	Biograph mCT Flow	3:1	2.2	-	-	x	PSF at FWHM (mm) (2 to 12)
Willowson et al. [44] (The QUEST study)	Various*	8:1	N/A	-	x	-	-
Strydhorst et al. [55]	Biograph mCT	8:1	N/A	x	-	-	-
D'Arienzo et al. [56]	Discovery ST	8:1	2.28	-	x	x	-
Siman et al. [36]	Discovery 690	4:1 13:1	1.6 4.8	-	x	x	OSEM (i1 to i12, 0mm, 2.6mm, 5.2mm, 7.8mm, 10.4mm)
Maughan et al. [58] (The MR-QUEST study)	Biograph mMR**	8:1	N/A	-	x	-	-
Scott and McGowan [59]	Discovery 710	8:1	N/A	x	x	-	PL
Rowley et al. [57]	Discovery 710	8:1	3.3	x	-	-	PL
Seo et al. [60]	SIGNA (PET/MR)	4:1	N/A	x	-	-	-
Hou et al. [61]	Discovery 690	7.5:1	2.45	x	x	x	PL
The present study	Vereos DPC	9:1	2.25	-	x	x	OSEM (i1, i2, i3, s10, s20, s30, 0mm, 2mm, 4mm, 6mm, 8mm 5, 10, 15 min/bed)

**Table 5** Summary of phantom studies with hot spheres for  $^{90}\text{Y}$ , for several PET/CT and PET/MR systems, SBR and  $AC_{ref}$ . The four last columns to the right summarise the type of evaluation done in the different studies. Contrast: Qualitative evaluation using definitions such as in the NEMA NU-2 standards for image quality. Activity: Quantitative evaluation either based on activity or  $RC_{AC}$  estimates. Dose: Quantitative evaluation based on  $RC_{Dose}$  or DVH. Optim: Studies which aimed at varying reconstruction parameters to find optimised reconstruction parameters. Only variable parameters for OSEM reconstructions with ToF are described.

\*The QUEST phantom study including 69 PET/CT systems (GE, Siemens, Philips)

\*\* The MR-QUEST phantom study including 8 PET/MR systems (Siemens)

*DVH comparisons using RMSD.* We evaluated the reconstruction parameters using RMSD comparisons between DVHs as suggested by Siman *et al.*, but this could not be a relevant criteria for assessing absorbed dose distributions. Variations in RMSD will be observed depending on the range chosen for calculation, e.g.  $D_{0\%}$ - $D_{100\%}$ ,  $D_{10\%}$ - $D_{90\%}$  and  $D_{20\%}$ - $D_{80\%}$ , as explained by Siman *et al.* themselves. We chose to use the whole range ( $D_{0\%}$ - $D_{100\%}$ ) in our evaluation even if larger RMSD would be obtained to include all factors which could affect the dosimetry.

We find that the use of DVH is necessary and enough to make a choice on the reconstruction parameters. However, it depends on the information required ( $D_{mean}$ ,  $D_{max}$ ,  $D_{20\%}$ ,  $D_{50\%}$ ,  $D_{80\%}$ , etc.), and the size of the VOI. For example, for the 22-37 mm spheres in Figure 4, a compromise can be found between intermediate absorbed doses, e.g. between  $D_{20\%}$  and  $D_{80\%}$ , and the  $D_{max}$ , where 13s10-0mm (or 13s10-2mm) can be suitable for reconstruction.

*RC<sub>AC</sub> and RC<sub>Dose</sub>.* Owing to the few statistical production of positrons during  $^{90}\text{Y}$  decay, PVE and other confounding factors, the  $RC_{AC}$  do not reach 100% for the larger spheres of Ph3, as it can be the case for  $^{18}\text{F}$  imaging. This is true for all 69 PET systems evaluated in the QUEST multicentric study [44] in 2014, for any kind of reconstruction. No evaluation was performed on any SiPM system in the QUEST, owing that SiPM PET systems were commercialised as from 2013 for Philips, 2016 for GE and 2018 for Siemens. Since activity recovery is not reached at 100% for spheres up to 37 mm, the calculation of absorbed dose would be inaccurate and corrections in the absorbed dose estimation still need to be investigated and accounted for further post  $^{90}\text{Y}$ -SIRT dosimetry. For the largest 28 and 37 mm spheres, the  $RC_{Dose}$  were around 0.8, and the  $D_{pet}^{VSV}$  seems to be underestimated by about roughly 20% if we compare to  $D_{ref}^{MC}$ . The two smallest 10 and 13 mm spheres have underestimations on the mean absorbed dose which can be greater than 50%. The latter still suffer from greater PVE due to the spatial resolution which is around 4 mm FWHM [28–30]. In an attempt to compare to  $^{18}\text{F}$  imaging but for qualitative studies and diagnostic purposes, Salvadori *et al.* [37] obtained CRCs which were less than 50% using 1 to 3 OSEM iterations for the 10 mm sphere on the DPC-PET, showing the limits of small spheres even for high  $\beta^+$  production statistics.

*Absorbed dose calculation.* VSV convolution for absorbed dose calculation is based on pre-calculated kernels by Monte Carlo methods and has been validated and proved to be clinically suitable for  $^{90}\text{Y}$  post-SIRT dosimetry [68]. Monte Carlo simulations were used in this study but did not aim at replacing dosimetry by clinical VSV convolution. It was used as a tool to obtain our reference in absorbed dose distributions. It has not been detailed here, but absorbed dose distributions using VSV convolution were compared to PET image-based Monte Carlo simulations where excellent agreements were obtained between them, again illustrating the major image degradation coming from the non-ideal PET performance impacting on the absorbed dose distribution. VSV calculation is fast and clinically feasible for each patient (approx. 30 seconds per patient).

*Comparison to previous studies.* Following the improvements in photon detection in PET systems, PET/CT is becoming a benchmark for monitoring  $^{90}\text{Y}$  biodistribution following SIRT as it provides improved accuracy for dosimetry. A number of phantom studies have been performed with  $^{90}\text{Y}$  on different PET systems [22, 34–36, 44, 48–61]. They are summarised in Table 5. Some studies focused on qualitative and detection performances through image quality reports [34, 52, 54, 55, 57, 59–61], such as the CRC and the background variation (BV) following the NEMA NU-2 standards and guidelines [33]. Some other studies focused on a more quantitative evaluation on activity concentrations through  $RC_{AC}$  [22, 34, 36, 44, 48–51, 53, 56, 58, 59, 61]. Fewer phantom studies focused on improving dosimetric quantification through  $RC_{Dose}$  or other dosimetric clinical routine metrics [35, 36, 52, 56, 61]. Elschot *et al.* [52] in 2013 showed through DVH that  $^{90}\text{Y}$  dosimetry is more precise for PET than SPECT imaging. Strydhorst *et al.* [55] in 2016 showed in their study that the bremsstrahlung radiation had negligible effects on PET-image image quality using Monte Carlo simulations. D'Arienzo *et al.* [56] in 2017 concluded that the post-SIRT dosimetry is possible even in conditions of low statistics and high random fraction, granted that accurate PET calibration is performed and acquisition durations are sufficiently long. Pasciak *et al.* [35] in 2014, Siman *et al.* [36] in 2018 and the latest study in 2020 from Hou *et al.* [61] were the only studies which suggested optimised reconstruction algorithms parameters using either, or both,  $RC_{Dose}$  and DVH estimations on phantoms. However, the suggested OSEM parameters from Pasciak *et al.* [35] (i1s21-0mm + 4.5 mm FWHM PSF + ToF) were different from Siman *et al.* [36] (i3s12-5.2mm + PSF + ToF) and were for different PET systems. Hou *et al.* [61] evaluated reconstructions on GE systems using a Penalised Likelihood (PL) algorithm.

*Limitations.* In the present study, we evaluated several  $DVH_{pet}^{V,SV}$  for the acquisition in specific conditions (SBR of 9:1, isotropic image voxel size of 2 mm,  $AC_{ref}$  of 2.18 MBq.mL $^{-1}$ ). For further investigation, evaluations of  $DVH_{pet}^{V,SV}$  should be made for the different  $AC_{ref}$  present in the spheres at different imaging times and also by varying the image resolution, for example for voxels of 4 mm instead of 2 mm here. Evaluations varying SBR would require more experimental data, with a different experimental setup for each SBR. However, the results presented in our study can be useful in the choice of OSEM reconstruction parameters for example in studies such as published by Wei *et al.* [75], Levillain *et al.* [76] and Morán *et al.* [77] for better accuracy in absorbed dose calculation following  $^{90}\text{Y}$ -SIRT using the DPC-PET.

## 5 Conclusion

This study aimed at evaluating various parameters for  $^{90}\text{Y}$ -PET imaging with a DPC-PET Philips system for post-SIRT image-based dosimetry. To our knowledge, no previous study concerning the evaluation of acquisition and reconstruction parameters through DVHs have been published previously for SiPM PET systems. On overall, for dosimetry purposes, we recommend to apply a 2 mm FWHM post-reconstruction Gaussian filter size, which could reduce noise in the reconstructed image by keeping the same accuracy as when no filter is applied. The selected reconstruction parameter set could be i3s10-2mm for large spheres, but this choice

depends on the absorbed dose information required. This study can be useful in the choice of reconstruction parameters using the DPC-PET, depending on imaging conditions for  $^{90}\text{Y}$ . The acquisition duration can also be reduced from 15 to 10 min/bed for  $^{90}\text{Y}$ -SIRT with acceptable accuracy degradation in the absorbed dose distribution, improving patient comfort.

#### Declarations

##### Ethics approval and consent to participate

Not applicable.

##### Consent for publication

Informed written consent was obtained from all individual participants included in the study.

##### Availability of data and materials

GATE scripts for simulation during the current study are available from the corresponding author on request.

##### Competing interest

The authors declare that they have no competing interests.

##### Funding

This work was supported in part by Philips Healthcare. This work was performed within the framework of the SIRIC LYriCAN Grant INCa-INSERM-DGOS-12563, and the LABEX PRIMES (ANR-11-LABX-0063) of Université de Lyon, within the program “Investissements d’Avenir” (ANR- 11-IDEX-0007) operated by the ANR.

##### Author’s contributions

JL, JNB, PB, PVD and FK performed most of the experimental acquisitions. JL performed all Monte Carlo simulations. JL and TB implemented all Python tools for data analysis. JL, DS, JNB and PB wrote most of the text. JL, DS and JNB initiated the project and defined the method. All authors read, corrected and approved the final manuscript.

##### Acknowledgements

The authors would like to thank Belinda Stiles (St. George’s University Hospitals, London, UK), Tony Younes (IUCT-Oncopole, Toulouse, France) and Julien Salvadori (IADI Laboratory, Nancy, France) for helpful review of the article.

##### Author details

<sup>1</sup>CREATIS; CNRS UMR 5220; INSERM U 1044; Université de Lyon; INSA-Lyon; Université Lyon 1, Lyon, France.

<sup>2</sup>Centre de lutte contre le cancer Léon Bérard, Lyon, France. <sup>3</sup>Hospices Civils de Lyon; Université de Lyon;

Université Claude Bernard Lyon 1; LAGEPP UMR 5007 CNRS, Lyon, France.

##### References

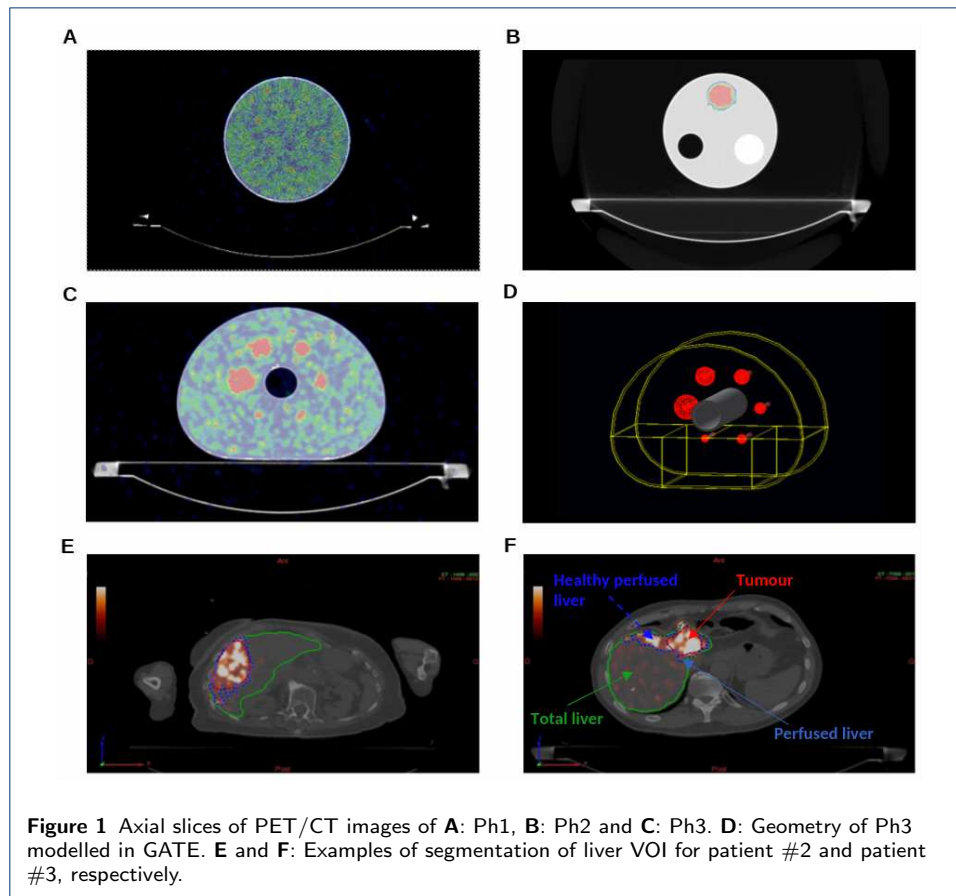
- Salem, R., Lewandowski, R.J., Mulcahy, M.F., Riaz, A., Ryu, R.K., Ibrahim, S., Atassi, B., Baker, T., Gates, V., Miller, F.H., *et al.*: Radioembolization for hepatocellular carcinoma using Yttrium-90 microspheres: a comprehensive report of long-term outcomes. *Gastroenterology* **138**(1), 52–64 (2010)
- Sangro, B., Carpanese, L., Cianni, R., Golfieri, R., Gasparini, D., Ezziddin, S., Paprottka, P.M., Fiore, F., Van Buskirk, M., Ignacio Bilbao, J., *et al.*: Survival after yttrium-90 resin microsphere radioembolization of hepatocellular carcinoma across Barcelona clinic liver cancer stages: a European evaluation. *Hepatology* **54**(3), 868–878 (2011)
- Lau, W., Leung, W., Ho, S., Leung, N., Chan, M., Lin, J., Metreweli, C., Johnson, P., Li, A.: Treatment of inoperable hepatocellular carcinoma with intrahepatic arterial yttrium-90 microspheres: a phase I and II study. *British Journal of Cancer* **70**(5), 994–999 (1994)
- Sato, K.T., Lewandowski, R.J., Mulcahy, M.F., Atassi, B., Ryu, R.K., Gates, V.L., Nemcek Jr, A.A., Barakat, O., Benson III, A., Mandal, R., *et al.*: Unresectable chemorefractory liver metastases: radioembolization with  $^{90}\text{Y}$  microspheres—safety, efficacy, and survival. *Radiology* **247**(2), 507–515 (2008)
- Kennedy, A.S., McNeillie, P., Dezarn, W.A., Nutting, C., Sangro, B., Wertman, D., Garafalo, M., Liu, D., Coldwell, D., Savin, M., *et al.*: Treatment parameters and outcome in 680 treatments of internal radiation with resin  $^{90}\text{Y}$ -microspheres for unresectable hepatic tumors. *International Journal of Radiation Oncology Biology Physics* **74**(5), 1494–1500 (2009)
- Cremonesi, M., Chiesa, C., Strigari, L., Ferrari, M., Botta, F., Guerriero, F., De Cicco, C., Bonomo, G., Orsi, F., Bodei, L., *et al.*: Radioembolization of hepatic lesions from a radiobiology and dosimetric perspective. *Frontiers in Oncology* **4**, 210 (2014)
- Garin, E., Rolland, Y., Laffont, S., Edeline, J.: Clinical impact of ( $^{99\text{m}}\text{Tc}$ -MAA SPECT/CT)-based dosimetry in the radioembolization of liver malignancies with  $^{90}\text{Y}$ -loaded microspheres. *European Journal of Nuclear Medicine and Molecular Imaging* **43**(3), 559–575 (2016)
- Haste, P., Tann, M., Persohn, S., LaRoche, T., Aaron, V., Mauxion, T., Chauhan, N., Dreher, M.R., Johnson, M.S.: Correlation of Technetium-99m Macroaggregated Albumin and Yttrium-90 Glass Microsphere Biodistribution in Hepatocellular Carcinoma: A Retrospective Review of Pretreatment Single Photon Emission CT and Posttreatment Positron Emission Tomography/CT. *Journal of Vascular and Interventional Radiology* **28**(5), 722–730 (2017)

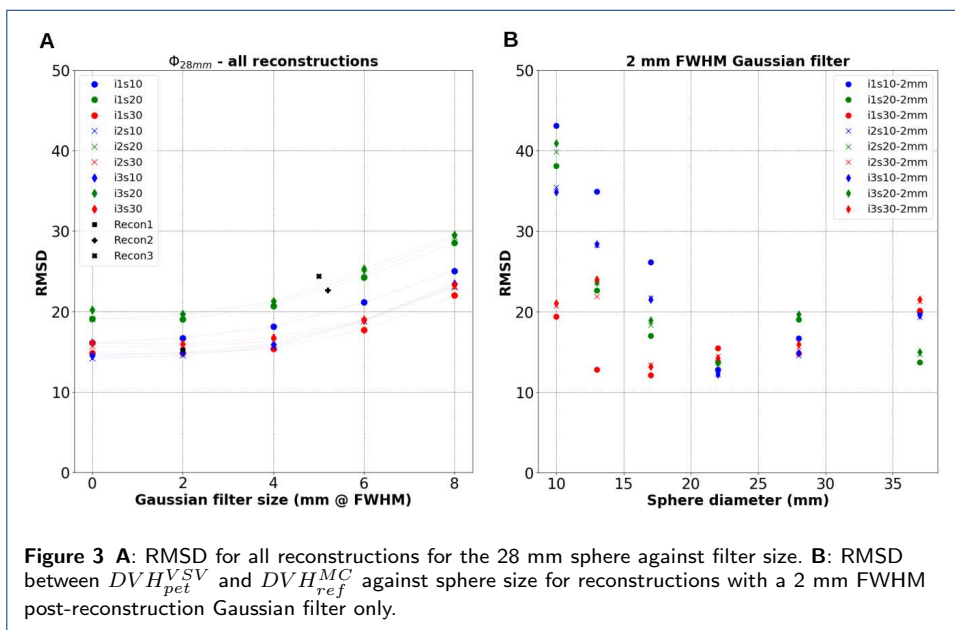
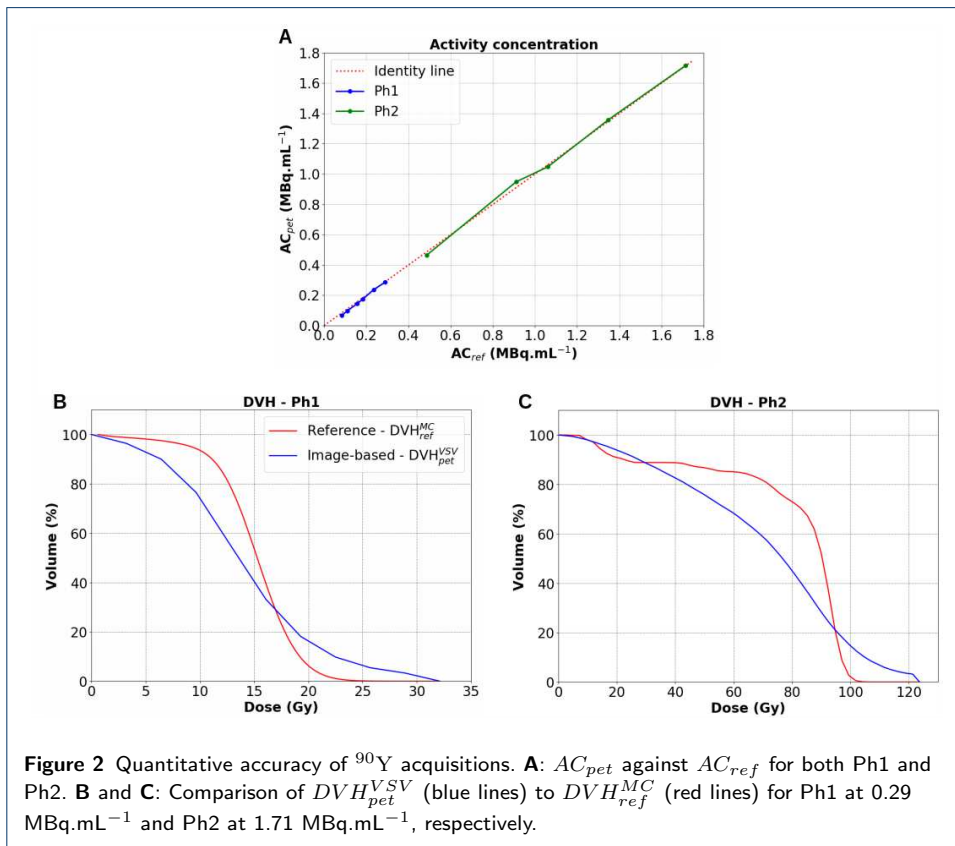
9. Richetta, E., Pasquino, M., Poli, M., Cutaia, C., Valero, C., Tabone, M., Paradisi, B.P., Pacilio, M., Pellerito, R.E., Stasi, M.: PET-CT post therapy dosimetry in radioembolization with resin  $^{90}\text{Y}$  microspheres: Comparison with pre-treatment SPECT-CT  $^{99\text{m}}\text{Tc}$ -MAA results. *Physica Medica* **64**, 16–23 (2019)
10. Dezarn, W., Cessna, J., DeWerd, L., Feng, W., Gates, V., Halama, J., Kennedy, A., Nag, S., Sarfaraz, M., Sehgal, V., Selwyn, R., Stabin, M., Thomadsen, B., Williams, L., Salem, R.: Recommendations of the American Association of Physicists in Medicine on dosimetry, imaging, and quality assurance procedures for  $^{90}\text{Y}$  microsphere brachytherapy in the treatment of hepatic malignancies. *Med. Phys.* **38**(8), 4824 (2011)
11. Walrand, S., Hesse, M., Demonceau, G., Pauwels, S., Jamar, F.: Yttrium-90-labeled microsphere tracking during liver selective internal radiotherapy by bremsstrahlung pinhole SPECT: feasibility study and evaluation in an abdominal phantom. *EJNMMI Research* **1**(1), 32 (2011)
12. Johnson, O., Johnson, R., Langer, L.: Evidence for a  $0+$  first excited state in  $\text{Zr}^{90}$ . *Physical Review* **98**(5), 1517 (1955)
13. Ford, K.W.: Predicted  $0+$  Level in  $\text{Zr}^{90}$ . *Physical Review* **98**(5), 1516 (1955)
14. Greenberg, J.S., Deutsch, M.: Positrons from the decay of  $\text{P}^{32}$  and  $\text{Y}^{90}$ . *Physical Review* **102**(2), 415 (1956)
15. Moore, C.F., Zaidi, S., Kent, J.: Single-Particle States Built on the Second  $0+$  State in  $\text{Zr}^{90}$ . *Physical Review Letters* **18**(10), 345 (1967)
16. Selwyn, R., Nickles, R., Thomadsen, B., DeWerd, L., Micka, J.: A new internal pair production branching ratio of  $^{90}\text{Y}$ : The development of a non-destructive assay for  $^{90}\text{Y}$  and  $^{90}\text{Sr}$ . *Applied Radiation and Isotopes* **65**(3), 318–327 (2007)
17. Dryák, P., Šolc, J.: Measurement of the branching ratio related to the internal pair production of Y-90. *Applied Radiation and Isotopes* **156**, 108942 (2020)
18. Nickles, R.J., Roberts, A.D., Nye, J.A., Converse, A.K., Barnhart, T.E., Avila-Rodriguez, M., Sundaresan, R., Dick, D.W., Hammas, R., Thomadsen, B.: Assaying and PET imaging of Yttrium-90:  $1 \gg 34 \text{ ppm} > 0$ . In: *IEEE Symposium Conference Record Nuclear Science 2004.*, vol. 6, pp. 3412–3414 (2004). IEEE
19. Lhommel, R., Goffette, P., Van den Eynde, M., Jamar, F., Pauwels, S., Bilbao, J.I., Walrand, S.: Yttrium-90 TOF PET scan demonstrates high-resolution biodistribution after liver SIRT. *European Journal of Nuclear Medicine and Molecular Imaging* **36**(10), 1696–1696 (2009)
20. Lhommel, R., Van Elmbt, L., Goffette, P., Van den Eynde, M., Jamar, F., Pauwels, S., Walrand, S.: Feasibility of  $^{90}\text{Y}$  TOF PET-based dosimetry in liver metastasis therapy using SIR-Spheres. *European Journal of Nuclear Medicine and Molecular Imaging* **37**(9), 1654–1662 (2010)
21. Elschot, M., Nijssen, J.F.W., Dam, A.J., de Jong, H.W.A.M.: Quantitative evaluation of scintillation camera imaging characteristics of isotopes used in liver radioembolization. *PLoS One* **6**(11) (2011)
22. Carlier, T., Eugène, T., Bodet-Milin, C., Garin, E., Ansquer, C., Rousseau, C., Ferrer, L., Barbet, J., Schoenahl, F., Kraeber-Bodéré, F.: Assessment of acquisition protocols for routine imaging of Y-90 using PET/CT. *EJNMMI Research* **3**(1), 1–12 (2013)
23. Gates, V.L., Esmail, A.A., Marshall, K., Spies, S., Salem, R.: Internal pair production of  $^{90}\text{Y}$  permits hepatic localization of microspheres using routine PET: proof of concept. *Journal of Nuclear Medicine* **52**(1), 72–76 (2011)
24. Kao, Y., Tan, E., Lim, K., Ng, C., Goh, S.: Yttrium-90 internal pair production imaging using first generation PET/CT provides high-resolution images for qualitative diagnostic purposes. *The British Journal of Radiology* **85**(1015), 1018–1019 (2012)
25. Kao, Y.-H., Steinberg, J.D., Tay, Y.-S., Lim, G.K., Yan, J., Townsend, D.W., Takano, A., Burgmans, M.C., Irani, F.G., Teo, T.K., *et al.*: Post-radioembolization Yttrium-90 PET/CT-part 1: diagnostic reporting. *EJNMMI Research* **3**(1), 56 (2013)
26. Lecoq, P.: Pushing the limits in time-of-flight PET imaging. *IEEE Transactions on Radiation and Plasma Medical Sciences* **1**(6), 473–485 (2017)
27. Gundacker, S., Turtos, R.M., Kratochwil, N., Pots, R.H., Paganoni, M., Lecoq, P., Auffray, E.: Experimental time resolution limits of modern SiPMs and TOF-PET detectors exploring different scintillators and Cherenkov emission. *Physics in Medicine & Biology* **65**(2), 025001 (2020)
28. Zhang, J., Maniowski, P., Knopp, M.V.: Performance evaluation of the next generation solid-state digital photon counting PET/CT system. *EJNMMI Research* **8**(1), 97 (2018)
29. Rausch, I., Ruiz, A., Valverde-Pascual, I., Cal-González, J., Beyer, T., Carrio, I.: Performance evaluation of the Vereos PET/CT system according to the NEMA NU2-2012 standard. *Journal of Nuclear Medicine* **60**(4), 561–567 (2019)
30. Salvadori, J., Labour, J., Odille, F., Marie, P.-Y., Badel, J.-N., Imbert, L., Sarrut, D.: Monte Carlo simulation of digital photon counting PET. *EJNMMI Physics* **7**, 1–19 (2020)
31. Van Sluis, J., De Jong, J., Schaar, J., Noordzij, W., Van Snick, P., Dierckx, R., Borra, R., Willemsen, A., Boellaard, R.: Performance characteristics of the digital Biograph Vision PET/CT system. *Journal of Nuclear Medicine* **60**(7), 1031–1036 (2019)
32. Chicheportiche, A., Marciano, R., Orevi, M.: Comparison of NEMA characterizations for Discovery MI and Discovery MI-DR TOF PET/CT systems at different sites and with other commercial PET/CT systems. *EJNMMI Physics* **7**(1), 4 (2020)
33. National Electrical Manufacturers Association (NEMA): NEMA Standards Publication NU 2-2018. Performance Measurements of Positron Emission Tomographs. Rosslyn, USA (2018). National Electrical Manufacturers Association (NEMA)
34. Willowson, K., Forwood, N., Jakoby, B.W., Smith, A.M., Bailey, D.L.: Quantitative  $^{90}\text{Y}$  image reconstruction in PET. *Medical Physics* **39**(11), 7153–7159 (2012)
35. Pasciak, A.S., Bourgeois, A.C., Bradley, Y.C.: A comparison of techniques for  $^{90}\text{Y}$  PET/CT image-based dosimetry following radioembolization with resin microspheres. *Frontiers in Oncology* **4**, 121 (2014)
36. Siman, W., Mikell, J.K., Mawlawi, O.R., Mourtada, F., Kappadath, S.C.: Dose volume histogram-based optimization of image reconstruction parameters for quantitative  $^{90}\text{Y}$ -PET imaging. *Medical Physics* **46**(1), 229–237 (2019)

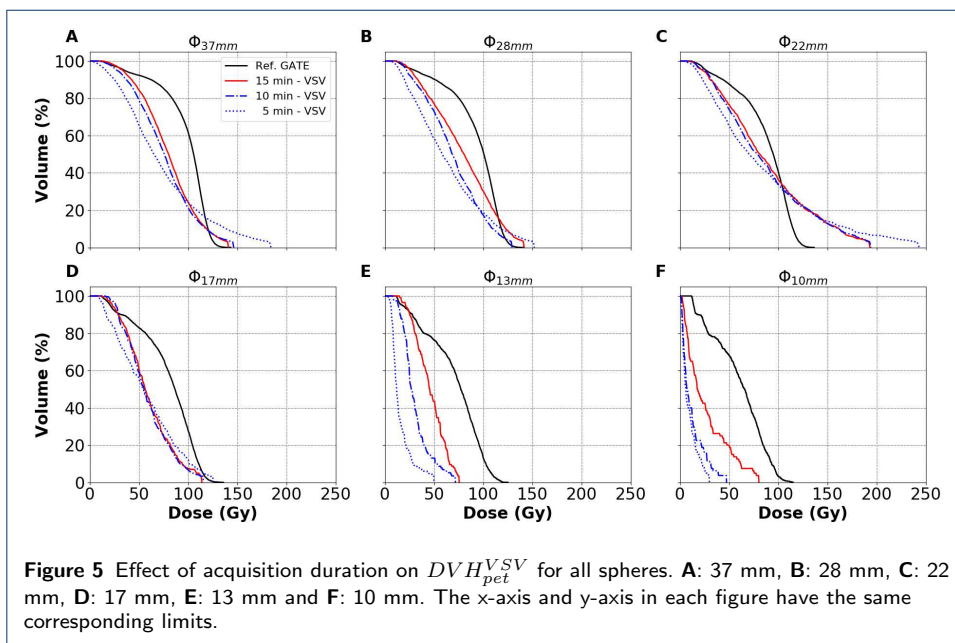
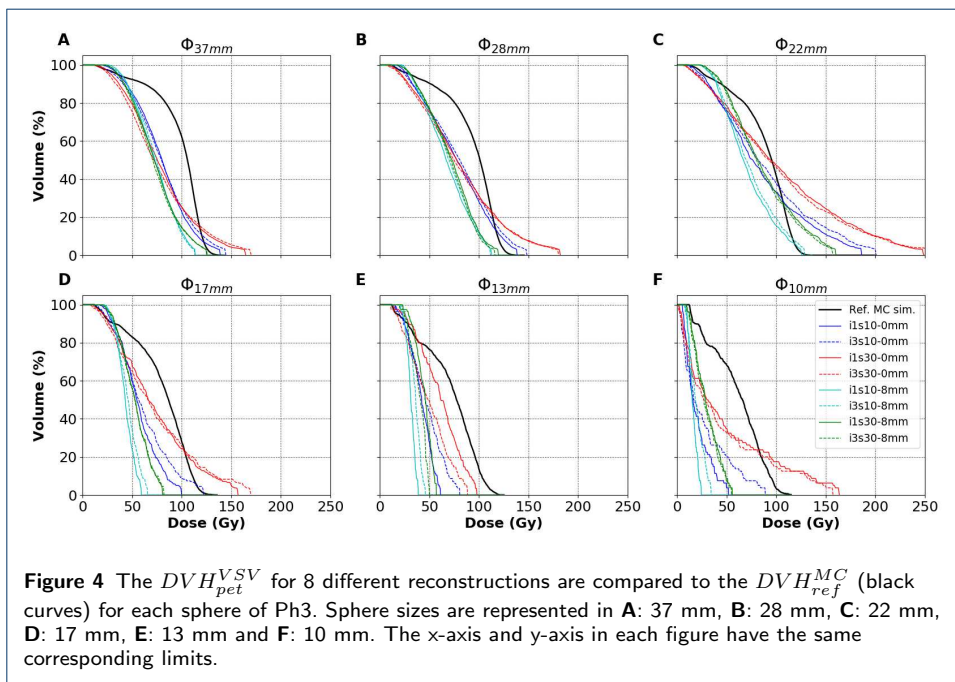
37. Salvadori, J., Odille, F., Verger, A., Olivier, P., Karcher, G., Marie, P.-Y., Imbert, L.: Head-to-head comparison between digital and analog PET of human and phantom images when optimized for maximizing the signal-to-noise ratio from small lesions. *EJNMMI Physics* **7**(1), 1–14 (2020)
38. Wright, C.L., Zhang, J., Binzel, K., Wuthrick, E.J., Knopp, M.V.:  $^{90}\text{Y}$  Digital PET/CT Imaging Following Radioembolization. *Clinical Nuclear Medicine* **41**(12), 975–976 (2016)
39. Wright, C.L., Binzel, K., Zhang, J., Wuthrick, E.J., Knopp, M.V.: Clinical feasibility of  $^{90}\text{Y}$  digital PET/CT for imaging microsphere biodistribution following radioembolization. *European Journal of Nuclear Medicine and Molecular Imaging* **44**(7), 1194–1197 (2017)
40. Wright, C., Binzel, K., Zhang, J., Wuthrick, E., Miller, E., Knopp, M.: Yttrium-90 imaging with digital photon counting pet/ct: An intra-individual comparison with conventional photomultiplier tube-based pet/ct following radioembolization. *Journal of Nuclear Medicine* **59**(supplement 1), 600–600 (2018)
41. Wang, W., Hu, Z., Gualtieri, E., Parma, M., Walsh, E., Sebok, D., Hsieh, Y.-L., Tung, C.-H., Song, X., Griesmer, J., et al.: Systematic and distributed time-of-flight list mode PET reconstruction. In: 2006 IEEE Nuclear Science Symposium Conference Record, vol. 3, pp. 1715–1722 (2006). IEEE
42. Narayanan, M., Perkins, A.: Resolution recovery in the Ingenuity TF PET/CT. White Paper, Philips NM Clinical Science (2013)
43. Drzymala, R., Mohan, R., Brewster, L., Chu, J., Goitein, M., Harms, W., Urie, M.: Dose-volume histograms. *International Journal of Radiation Oncology Biology Physics* **21**(1), 71–78 (1991)
44. Willowson, K.P., Tapner, M., Bailey, D.L., et al.: A multicentre comparison of quantitative  $^{90}\text{Y}$  PET/CT for dosimetric purposes after radioembolization with resin microspheres. *European Journal of Nuclear Medicine and Molecular Imaging* **42**(8), 1202–1222 (2015)
45. Richardson, W.H.: Bayesian-based iterative method of image restoration. *JoSA* **62**(1), 55–59 (1972)
46. Lucy, L.B.: An iterative technique for the rectification of observed distributions. *The Astronomical Journal* **79**, 745 (1974)
47. Golla, S., Lammertsma, A., Boellaard, R.: Performance of the resolution recovery method on the Ingenuity PET/CT. *Journal of Nuclear Medicine* **56**(supplement 3), 1836–1836 (2015)
48. Werner, M.K., Brechtel, K., Beyer, T., Dittmann, H., Pfannenberger, C., Kupferschläger, J.: PET/CT for the assessment and quantification of  $^{90}\text{Y}$  biodistribution after selective internal radiotherapy (SIRT) of liver metastases. *European Journal of Nuclear Medicine and Molecular Imaging* **37**(2), 407–408 (2010)
49. Van Elmbt, L., Vandenberghe, S., Walrand, S., Pauwels, S., Jamar, F.: Comparison of Yttrium-90 quantitative imaging by TOF and non-TOF PET in a phantom of liver selective internal radiotherapy. *Physics in Medicine & Biology* **56**(21), 6759 (2011)
50. Bagni, O., D'Arienzo, M., Chiamida, P., Chiacchiararelli, L., Cannas, P., D'Agostini, A., Cianni, R., Salvatori, R., Scopinaro, F.:  $^{90}\text{Y}$ -PET for the assessment of microsphere biodistribution after selective internal radiotherapy. *Nuclear Medicine Communications* **33**(2), 198–204 (2012)
51. D'Arienzo, M., Chiamida, P., Chiacchiararelli, L., Coniglio, A., Cianni, R., Salvatori, R., Ruzza, A., Scopinaro, F., Bagni, O.:  $^{90}\text{Y}$  PET-based dosimetry after selective internal radiotherapy treatments. *Nuclear Medicine Communications* **33**(6), 633–640 (2012)
52. Elschot, M., Vermolen, B.J., Lam, M.G., de Keizer, B., van den Bosch, M.A., de Jong, H.W.: Quantitative comparison of PET and Bremsstrahlung SPECT for imaging the in vivo Yttrium-90 microsphere distribution after liver radioembolization. *PLoS one* **8**(2) (2013)
53. Attarwala, A.A., Molina-Duran, F., Büsing, K.-A., Schönberg, S.O., Bailey, D.L., Willowson, K., Glatting, G.: Quantitative and qualitative assessment of Yttrium-90 PET/CT imaging. *PLoS one* **9**(11) (2014)
54. Martí-Climent, J.M., Prieto, E., Elosúa, C., Rodríguez-Fraile, M., Domínguez-Prado, I., Vigil, C., García-Velloso, M.J., Arbizu, J., Peñuelas, I., Richter, J.A.: PET optimization for improved assessment and accurate quantification of  $^{90}\text{Y}$ -microsphere biodistribution after radioembolization. *Medical Physics* **41**(9), 092503 (2014)
55. Strydhorst, J., Carlier, T., Dieudonné, A., Conti, M., Buvat, I.: A GATE evaluation of the sources of error in quantitative  $^{90}\text{Y}$  PET. *Medical Physics* **43**(10), 5320–5329 (2016)
56. D'Arienzo, M., Pimpinella, M., Capogni, M., De Coste, V., Filippi, L., Spezi, E., Patterson, N., Mariotti, F., Ferrari, P., Chiamida, P., et al.: Phantom validation of quantitative  $^{90}\text{Y}$  PET/CT-based dosimetry in liver radioembolization. *EJNMMI Research* **7**(1), 94 (2017)
57. Rowley, L.M., Bradley, K.M., Boardman, P., Hallam, A., McGowan, D.R.: Optimization of image reconstruction for  $^{90}\text{Y}$  selective internal radiotherapy on a lutetium yttrium orthosilicate PET/CT system using a Bayesian Penalized Likelihood reconstruction algorithm. *Journal of Nuclear Medicine* **58**(4), 658–664 (2017)
58. Maughan, N.M., Eldib, M., Faul, D., Conti, M., Elschot, M., Knešarek, K., Leek, F., Townsend, D., DiFilippo, F.P., Jackson, K., et al.: Multi institutional quantitative phantom study of Yttrium-90 PET in PET/MRI: the MR-QUEST study. *EJNMMI Physics* **5**(1), 7 (2018)
59. Scott, N.P., McGowan, D.R.: Optimising quantitative  $^{90}\text{Y}$  PET imaging: an investigation into the effects of scan length and Bayesian Penalised Likelihood reconstruction. *EJNMMI Research* **9**(1), 40 (2019)
60. Seo, Y., Khalighi, M.M., Wangerin, K.A., Deller, T.W., Wang, Y.-H., Jivan, S., Kohi, M.P., Aggarwal, R., Flavell, R.R., Behr, S.C., et al.: Quantitative and Qualitative Improvement of Low-Count [ $^{68}\text{Ga}$ ] Citrate and [ $^{90}\text{Y}$ ] Microspheres PET Image Reconstructions Using Block Sequential Regularized Expectation Maximization Algorithm. *Molecular Imaging and Biology* **22**(1), 208–216 (2020)
61. Hou, X., Ma, H., Esquinas, P.L., Uribe, C.F., Tolhurst, S., Bénard, F., Liu, D., Rahmim, A., Celler, A.: Impact of image reconstruction method on dose distributions derived from  $^{90}\text{Y}$  PET images: phantom and liver radioembolization patient studies. *Physics in Medicine & Biology* (2020)
62. Jan, S., Benoit, D., Becheva, E., Carlier, T., Cassol, F., Descourt, P., Frisson, T., Grevillot, L., Guigues, L., Maigne, L., Morel, C., Perrot, Y., Rehfeld, N., Sarrut, D., Schaart, D.R., Stute, S., Pietrzyk, U., Visvikis, D., Zahra, N., Buvat, I.: GATE V6: A major enhancement of the GATE simulation platform enabling modelling of CT and radiotherapy. *Phys Med Biol* **56**(4), 881–901 (2011). doi:10.1088/0031-9155/56/4/001
63. Sarrut, D., Bardiès, M., Bousson, N., Freud, N., Jan, S., Létang, J.-M., Loudos, G., Maigne, L., Marcatili, S.,

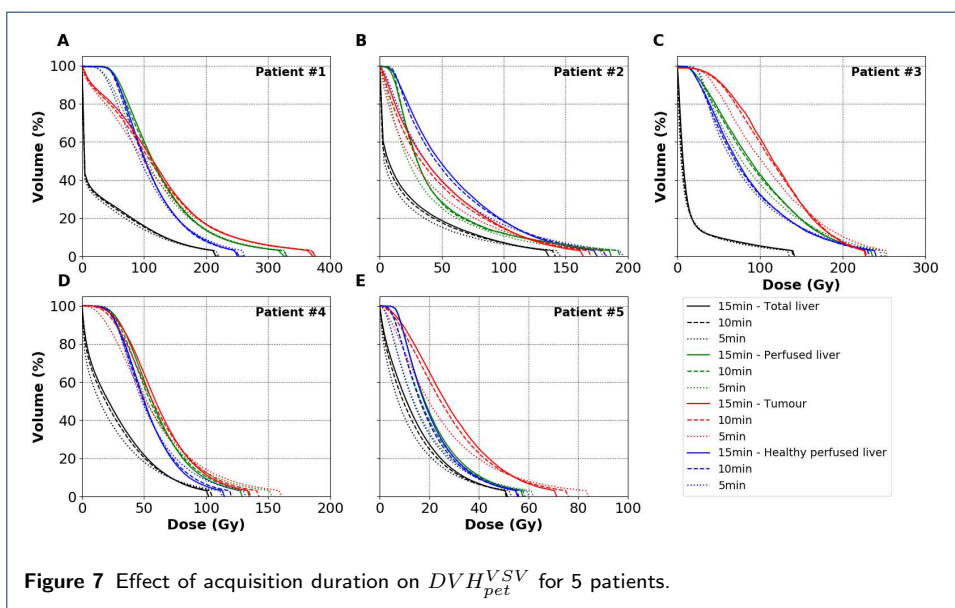
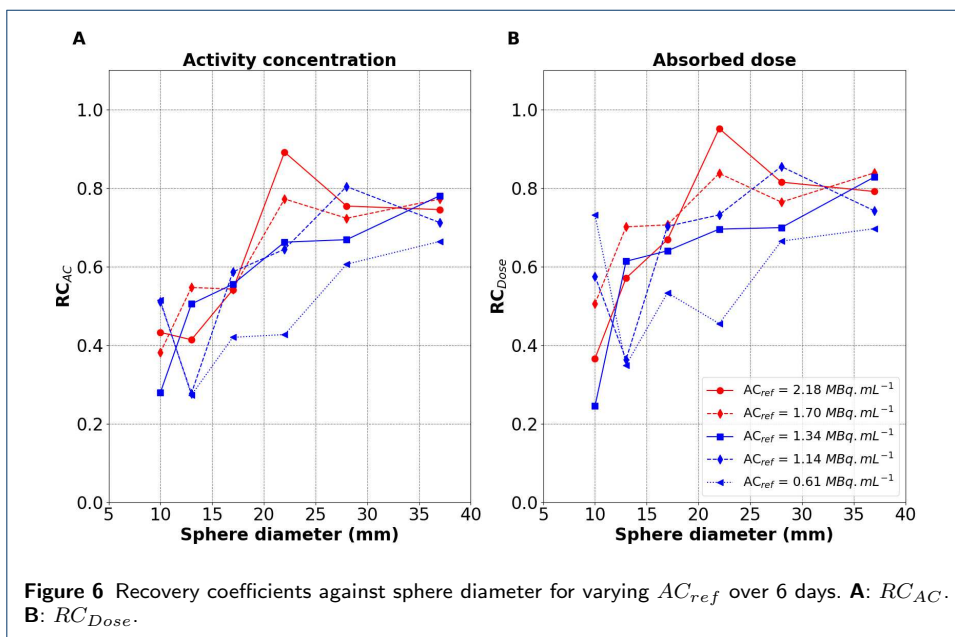
- Mauxion, T., *et al.*: A review of the use and potential of the GATE Monte Carlo simulation code for radiation therapy and dosimetry applications. *Medical Physics* **41**(6Part1) (2014)
64. Collaboration, G., Agostinelli, S., *et al.*: Geant4—a simulation toolkit. *Nucl. Instrum. Meth. A* **506**(25), 0 (2003)
  65. Beaudoux, V., Blin, G., Barbrel, B., Kantor, G., Zacharatou, C.: Geant4 physics list comparison for the simulation of phase-contrast mammography (XPulse project). *Phys Med* **60**, 66–75 (2019)
  66. Bolch, W.E., Eckerman, K.F., Sgouros, G., Thomas, S.R.: MIRDO pamphlet no. 21: a generalized schema for radiopharmaceutical dosimetry—standardization of nomenclature. *Journal of Nuclear Medicine* **50**(3), 477–484 (2009)
  67. Dieudonné, A., Hobbs, R.F., Bolch, W.E., Sgouros, G., Gardin, I.: Fine-resolution voxel S values for constructing absorbed dose distributions at variable voxel size. *Journal of nuclear medicine* **51**(10), 1600–1607 (2010)
  68. Dieudonné, A., Garin, E., Laffont, S., Rolland, Y., Lebtahi, R., Leguludec, D., Gardin, I.: Clinical feasibility of fast 3-dimensional dosimetry of the liver for treatment planning of hepatocellular carcinoma with <sup>90</sup>Y-microspheres. *Journal of Nuclear Medicine* **52**(12), 1930–1937 (2011)
  69. Gardin, I., Bouchet, L.G., Assié, K., Caron, J., Lisbona, A., Ferrer, L., Bolch, W.E., Vera, P.: Voxeldose: a computer program for 3-D dose calculation in therapeutic nuclear medicine. *Cancer Biotherapy and Radiopharmaceuticals* **18**(1), 109–115 (2003)
  70. Sarfaraz, M., Kennedy, A.S., Lodge, M.A., Li, X.A., Wu, X., Yu, C.X.: Radiation absorbed dose distribution in a patient treated with yttrium-90 microspheres for hepatocellular carcinoma. *Medical Physics* **31**(9), 2449–2453 (2004)
  71. Ferrari, M.E., Cremonesi, M., Di Dia, A., Botta, F., De Cicco, C., Sarnelli, A., Pedicini, P., Calabrese, M., Orecchia, R., Pedrolì, G., *et al.*: 3D dosimetry in patients with early breast cancer undergoing Intraoperative Avidiation for Radionuclide Therapy (IART®) combined with external beam radiation therapy. *European Journal of Nuclear Medicine and Molecular Imaging* **39**(11), 1702–1711 (2012)
  72. Ho, S., Lau, W., Leung, T., Chan, M., Ngar, Y., Johnson, P., Li, A.: Partition model for estimating radiation doses from yttrium-90 microspheres in treating hepatic tumours. *European Journal of Nuclear Medicine* **23**(8), 947–952 (1996)
  73. Vandendriessche, D., Uribe, J., Bertin, H., De Geeter, F.: Performance characteristics of silicon photomultiplier based 15-cm AFOV TOF PET/CT. *EJNMMI Physics* **6**(1), 8 (2019)
  74. Carlier, T., Ferrer, L., Conti, M., Bodet-Milin, C., Rousseau, C., Bercier, Y., Bendriem, B., Kraeber-Bodéré, F.: From a PMT-based to a SiPM-based PET system: a study to define matched acquisition/reconstruction parameters and NEMA performance of the Biograph Vision 450 (2020)
  75. Wei, L., Cui, C., Xu, J., Kaza, R., El Naqa, I., Dewaraja, Y.K.: Tumor Response Prediction in <sup>90</sup>Y Radioembolization with PET-based Radiomics Features and Absorbed Dose Metrics. *EJNMMI Physics* **7**(1) (2020)
  76. Levillain, H., Burghilea, M., Derijckere, I.D., Guiot, T., Gulyban, A., Vanderlinden, B., Vouche, M., Flamen, P., Reynaert, N.: Combined quality and dose-volume histograms for assessing the predictive value of <sup>99m</sup>Tc-MAA SPECT/CT simulation for personalizing radioembolization treatment in liver metastatic colorectal cancer. *EJNMMI Physics* **7**(1), 1–19 (2020)
  77. Morán, V., Prieto, E., Sancho, L., Rodríguez-Fraile, M., Soria, L., Zubiria, A., Martí-Climent, J.M.: Impact of the dosimetry approach on the resulting <sup>90</sup>Y radioembolization planned absorbed doses based on <sup>99m</sup>Tc-MAA SPECT-CT: is there agreement between dosimetry methods? *EJNMMI Physics* **7**(1), 1–22 (2020)

## Figures









# Figures

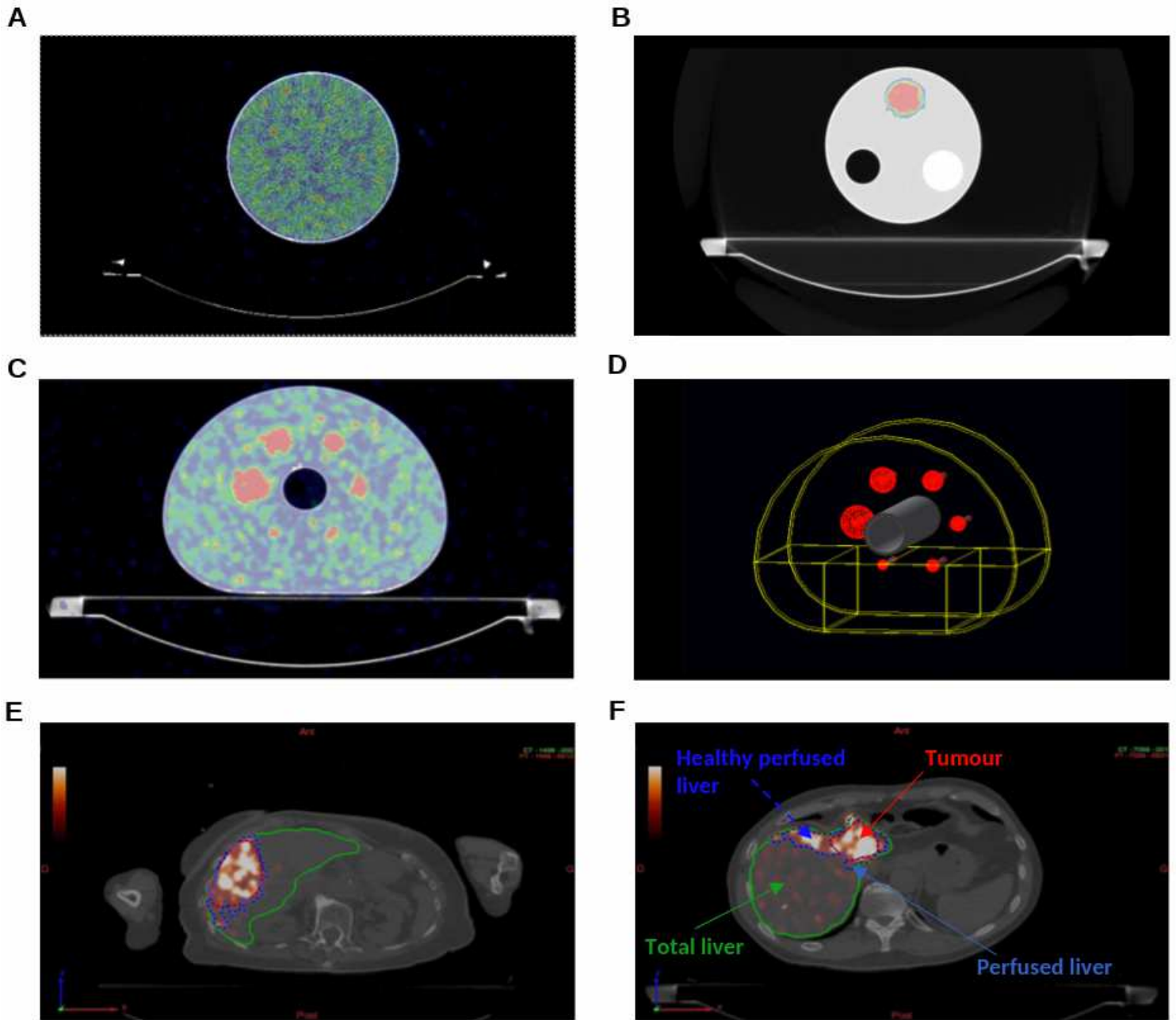


**Figure 1**

Axial slices of PET/CT images of A: Ph1, B: Ph2 and C: Ph3. D: Geometry of Ph3 modelled in GATE. E and F: Examples of segmentation of liver VOI for patient #2 and patient #3, respectively.

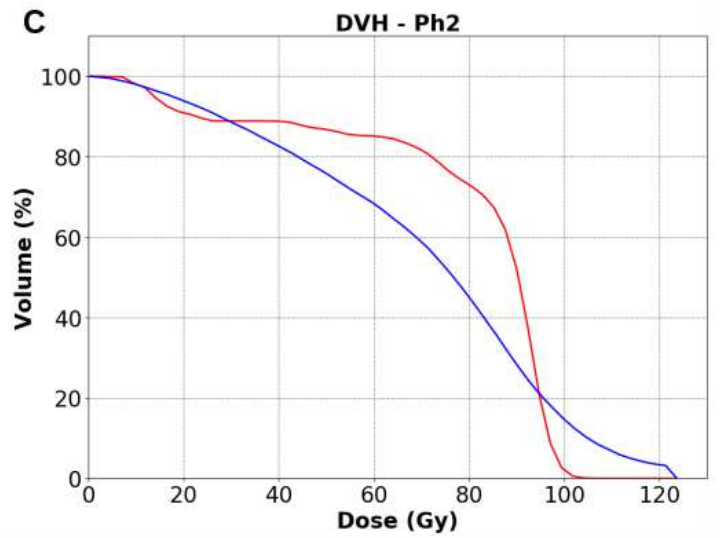
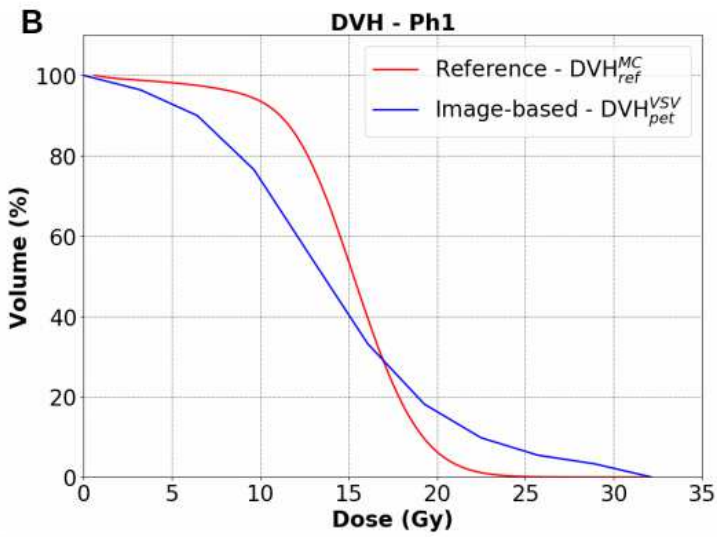
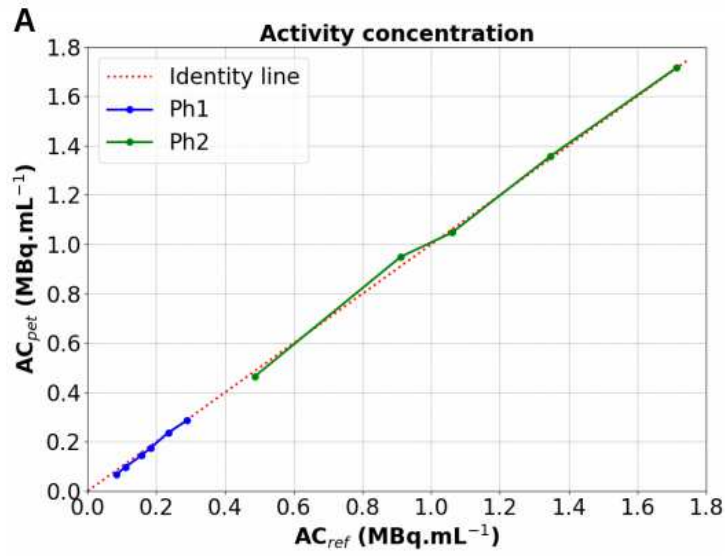


**Figure 2**

Please see the Manuscript PDF file for the complete figure caption.

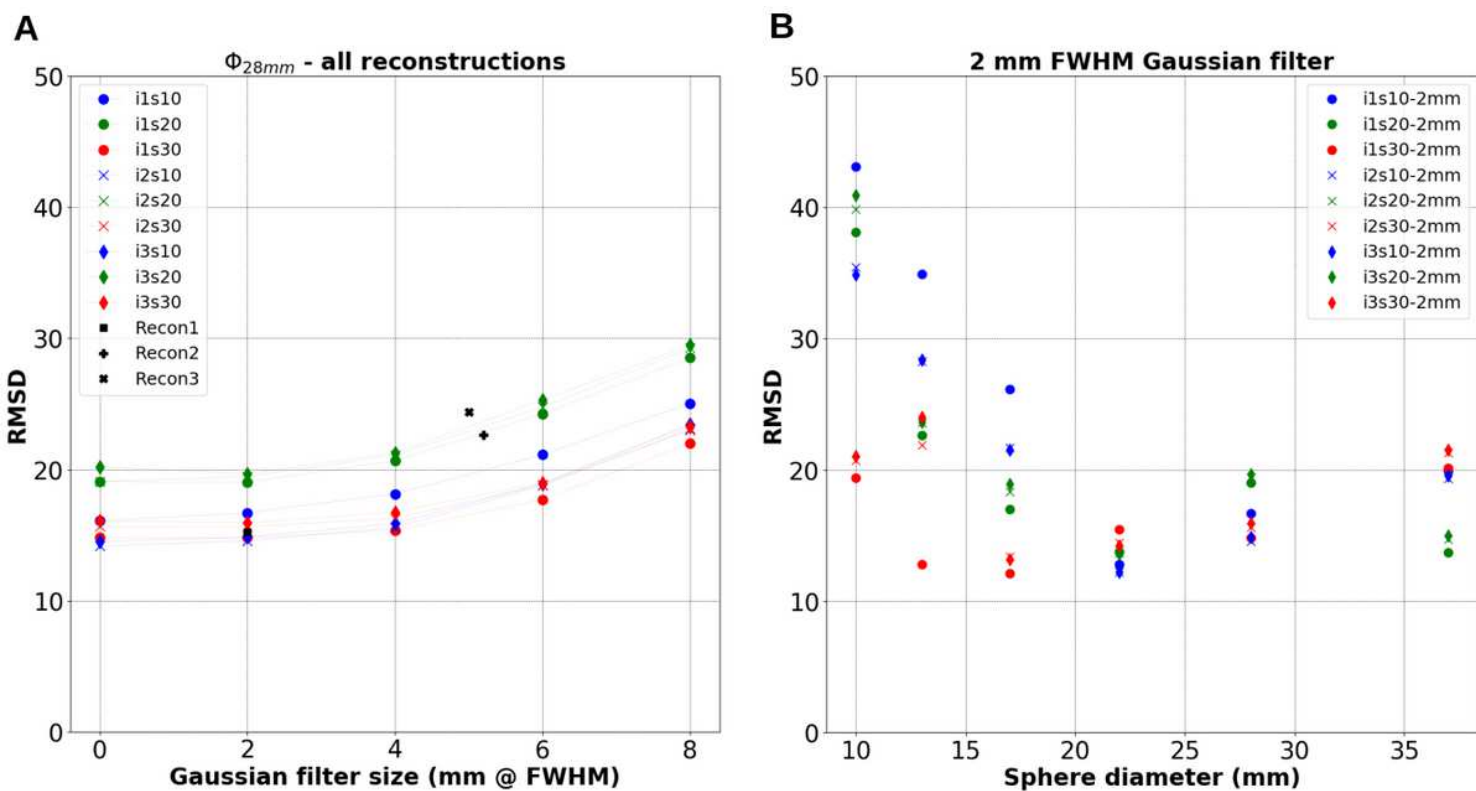


Figure 3

Please see the Manuscript PDF file for the complete figure caption.

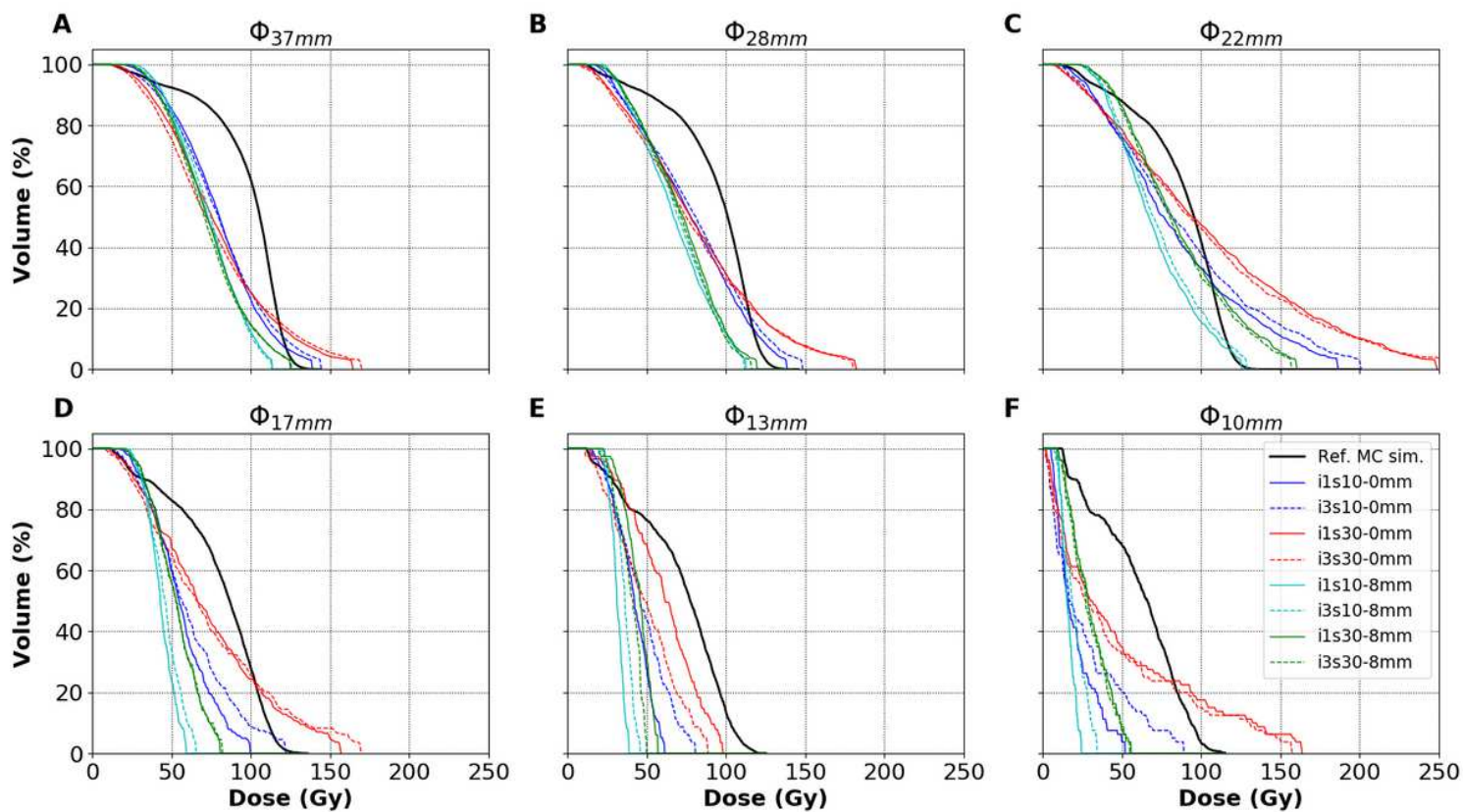


Figure 4

Please see the Manuscript PDF file for the complete figure caption.

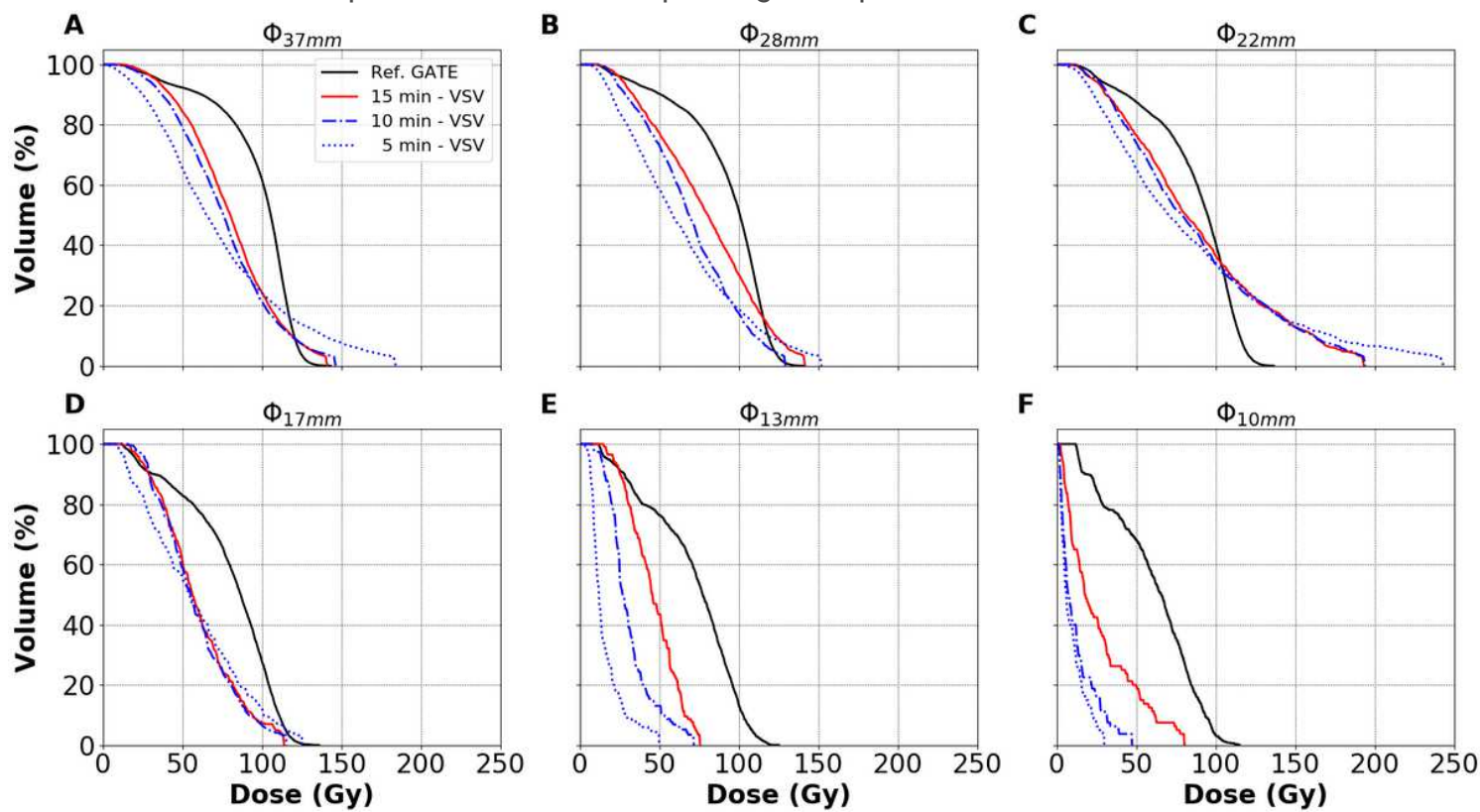


Figure 5

Please see the Manuscript PDF file for the complete figure caption.

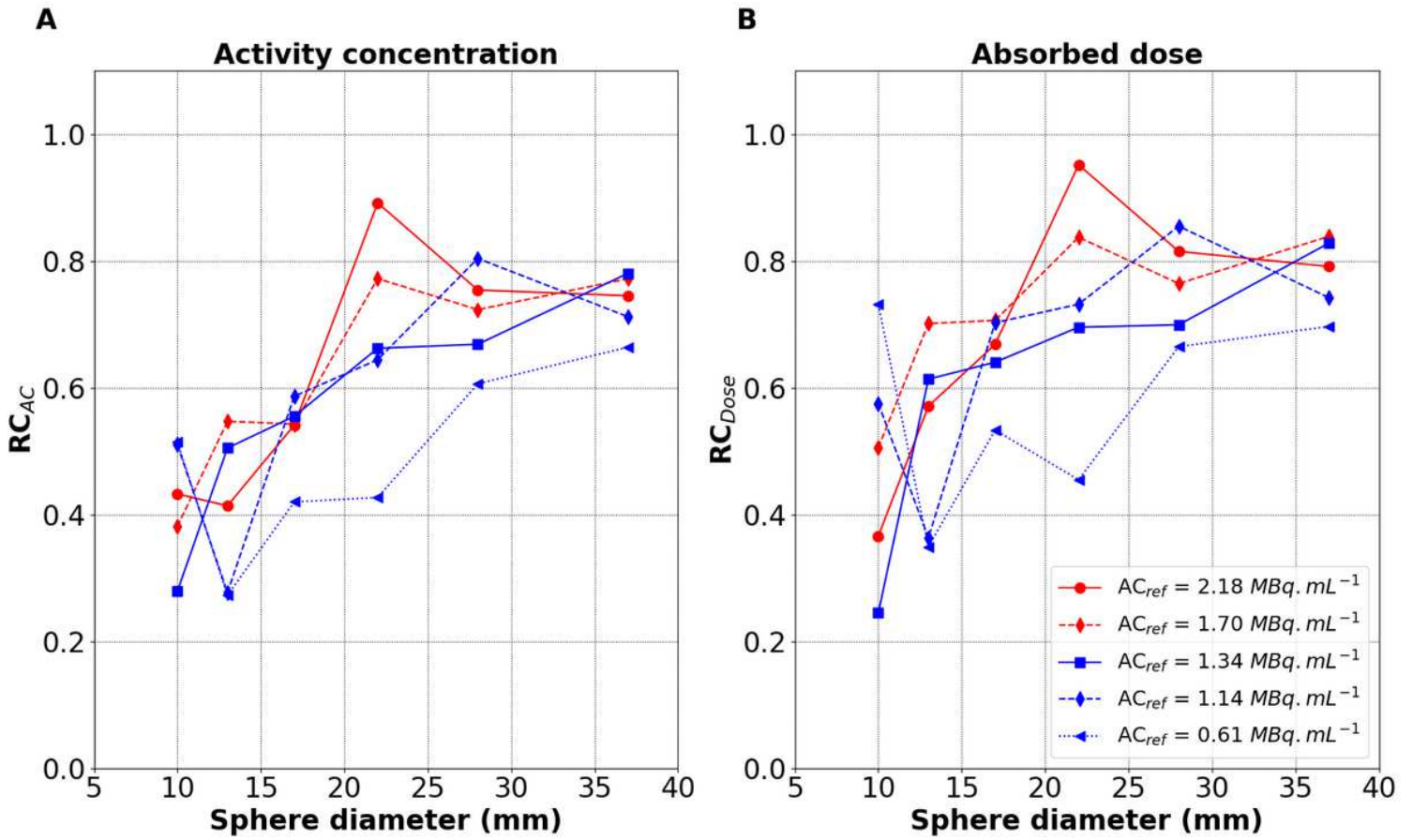
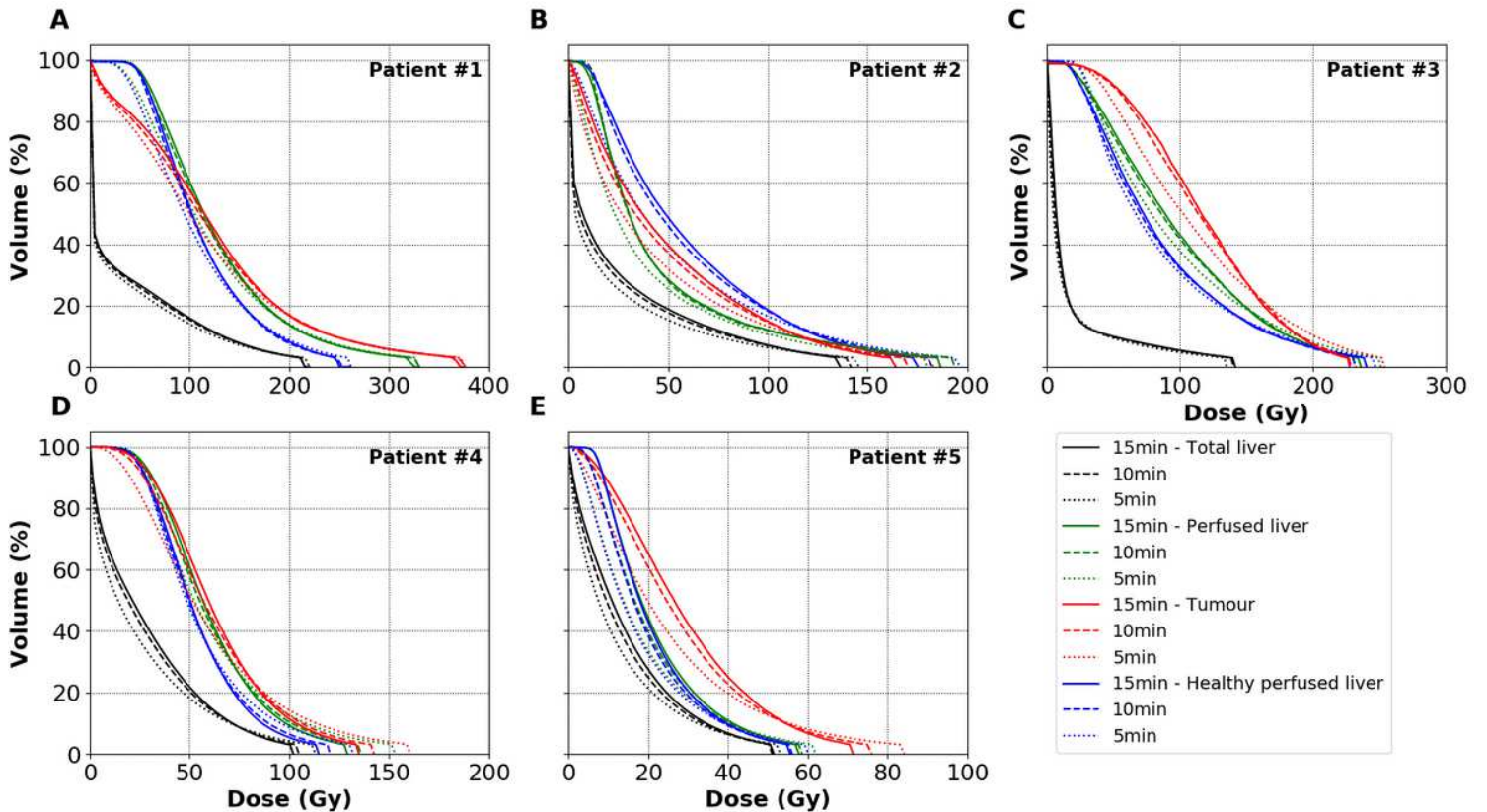


Figure 6

Recovery coefficients against sphere diameter for varying  $AC_{ref}$  over 6 days. A:  $RC_{AC}$ . B:  $RC_{Dose}$ .



## Figure 7

Please see the Manuscript PDF file for the complete figure caption.